The Astrophysical Journal, 584:76–99, 2003 February 10

A MULTIWAVELENGTH APPROACH TO THE STAR FORMATION RATE ESTIMATION IN GALAXIES AT INTERMEDIATE REDSHIFTS[1,2,3]

N. Cardiel,[4] D. Elbaz,[5,6] R. P. Schiavon, C. N. A. Willmer,[7] D. C. Koo,
A. C. Phillips, and J. Gallego[4]
University of California Observatories, Lick Observatory, University of California, Santa Cruz, CA 95064;
ncl@astrax.fis.ucm.es, elbaz@cea.fr, ripisc@ucolick.org, cnaw@ucolick.org,
koo@ucolick.org, phillips@ucolick.org, jgm@astrax.fis.ucm.es
Received 2002 May 17; accepted 2002 October 16

ABSTRACT

We use a sample of seven starburst galaxies at intermediate redshifts ($z \sim 0.4$ and 0.8) with observations ranging from the observed ultraviolet to 1.4 GHz, to compare the star formation rate (SFR) estimators that are used in the different wavelength regimes. We find that *extinction-corrected* Hα underestimates the SFR, and the degree of this underestimation increases with the infrared luminosity of the galaxies. Galaxies with very different levels of dust extinction as measured with $\mathrm{SFR_{IR}}/\mathrm{SFR}(\mathrm{H}\alpha$, uncorrected for extinction) present a similar attenuation $A[\mathrm{H}\alpha]$, as if the Balmer lines probed a different region of the galaxy than the one responsible for the bulk of the IR luminosity for large SFRs. In addition, SFR estimates derived from [O II] λ3727 match very well those inferred from Hα after applying the metallicity correction derived from local galaxies. SFRs estimated from the UV luminosities show a dichotomic behavior, similar to that previously reported by other authors in galaxies at $z \lesssim 0.4$. Here we extend this result up to $z \sim 0.8$. Finally, one of the studied objects is a luminous compact galaxy (LCG) that may be suffering similar dust-enshrouded star formation episodes. These results highlight the relevance of quantifying the actual L_{IR} of LCGs, as well as that of a much larger and generic sample of luminous infrared galaxies, which will be possible after the launch of *SIRTF*.

Subject headings: galaxies: evolution — galaxies: high-redshift — galaxies: starburst — galaxies: stellar content

On-line material: color figure

1. INTRODUCTION

The observational efforts devoted during the last years to measuring the cosmic star formation history are clearly manifest in the growing number of works in the field. As a result of the advent of the *Hubble Space Telescope* (*HST*) and of the 8–10 m class telescopes, the rest-frame ultraviolet (UV) star formation history per unit comoving volume initially derived up to $z \sim 1$ (Lilly et al. 1996) was extended up to $z \sim 4$ (Madau et al. 1996; Steidel et al. 1999). Naturally, all these works rely on the use of the available star formation rate (SFR) diagnostics: nebular emission lines like Hα (Kennicutt 1992a, 1998; Gallego et al. 1995; Tresse & Maddox 1998; Glazebrook et al. 1999; Moorwood et al. 2000; Hopkins, Connolly, & Szalay 2000) and [O II] (Hogg et al. 1998; Aragón-Salamanca et al. 2002), UV continuum luminosities (Lilly et al. 1996; Madau et al. 1996; Treyer et al. 1998; Cowie, Songalia, & Barger 1999; Steidel et al. 1999; Sullivan et al. 2000, 2001), far-infrared (FIR) luminosities (Rowan-Robinson et al. 1997; Blain et al. 1999; Flores et al. 1999; Chary & Elbaz 2001), and 1.4 GHz radio luminosities (Condon 1992; Cram et al. 1998). Different cosmic star formation histories have been advocated from these various studies, which can only be reconciled if the effect of dust extinction is accounted for.

In the local universe, galaxies radiate the bulk of their luminosity in the stellar regime, i.e., below $\lambda \sim 5$ μm. On average, only about one-third of their stellar light is absorbed by dust and reemitted in the dust regime from the mid-infrared (MIR) to the submillimeter (Soifer & Neugebauer 1991). In the distant universe, the reverse seems to take place as suggested by the combined results of the *Cosmic Background Explorer* (*COBE*), the ISOCAM and ISOPHOT instruments on board the *Infrared Space Observatory* (*ISO*), and the submillimeter camera SCUBA at the JCMT. Number counts at 15 μm (Elbaz et al. 1999), at 90 and 170 μm (Efstathiou et al. 2000; Kawara et al. 2000; Matsuhara et al. 2000; Dole et al. 2001), and at 450 and 850 μm (Smail et al. 2002 and references therein) revealed the presence of an excess of faint galaxies by 1 order of magnitude in comparison with expectations based on the local properties of galaxies. Such excess can only be explained if galaxies emitted a larger fraction of their luminosity in the

[1] Based on data obtained at the W. M. Keck Observatory, which is operated as a scientific partnership among the California Institute of Technology, the University of California, and the National Aeronautics and Space Administration. The Observatory was made possible by the generous financial support of the W. M. Keck Foundation.

[2] Based in part on observations with the NASA/ESA *Hubble Space Telescope*, obtained at the Space Telescope Science Institute, which is operated by the Association of Universities for Research in Astronomy, Inc., under NASA contract NAS 5-26555.

[3] Based in part on observations with the *Infrared Space Observatory* (*ISO*), an ESA project with instruments funded by ESA Member States (especially the PI countries: France, Germany, Netherlands, and United Kingdom) with the participation of ISAS and NASA.

[4] Departamento de Astrofísica, Facultad de Físicas, Avenida Complutense s/n, 28040 Madrid, Spain.

[5] Centre d'Etudes de Saclay, Service d'Astrophysique, Batiment 709, Orme des Merisiers, 91191 Gif-sur-Yvette Cédex, France.

[6] Department of Physics, University of California, Santa Cruz, CA 95064.

[7] On leave from Observatório Nacional, Rua General José Cristino 77, São Cristovão, Rio de Janeiro, Brazil.

dust regime in the past. This conclusion is reinforced by the detection of a strong cosmic infrared background (CIRB) above $\lambda \sim 100$ μm (Puget et al. 1996; Hauser et al. 1998; Fixsen et al. 1998; Lagache et al. 1999, 2000), the bulk of which appears to be produced by starbursting galaxies radiating the majority of their light in the IR above $\lambda \sim 5$ μm (Elbaz et al. 2002; Chary & Elbaz 2001).

Two major questions remain unanswered:

1. How consistent are the different SFR indicators commonly used in the literature?
2. Do local and distant galaxies exhibit a similar behavior?

Studies of local galaxies have shown that even after correcting for dust extinction, a significant discrepancy remains between SFRs derived from UV and Hα measurements compared with those obtained from FIR and radio luminosities, as well as that this discrepancy is worse for galaxies with higher SFRs (Hopkins et al. 2001; Poggianti & Wu 2000). Hopkins et al. (2001) and Sullivan et al. (2001) report an increase of the $F(\mathrm{H}\alpha)/F(\mathrm{H}\beta)$ ratio, used to measure extinction, with the SFR of galaxies. They suggest to use the fit to this correlation in order to account for dust extinction when Hβ is not available. However, Buat et al. (2002) indicate that the apparent link between extinction and star formation is likely not real, but only the result of a dispersed correlation between dust extinction and luminosity.

In a recent paper, Rigopoulou et al. (2000) studied a sample of 12 galaxies with $0.4 < z < 1.4$, detected with ISOCAM in the Hubble Deep Field–South (HDF-S). They showed that the discrepancy found between optical–UV and FIR–radio SFRs in the local universe is also present at high z. However, the Balmer decrement was not available for these galaxies, and the authors discussed the effect of dust extinction assuming an average correction factor of 4 for SFR(Hα).

In this paper we propose to address the two previous questions using a test sample of seven galaxies at $z \sim 0.4$ and 0.8, five of which have MIR flux densities from which we derived FIR luminosities assuming that the correlation between MIR and FIR luminosities observed in the local universe remains valid at these redshifts (Elbaz et al. 2002; Chary & Elbaz 2001). The galaxies were selected from their MIR flux density in order to sample SFRs in the range from 2 to 160 $M_\odot$ yr^{-1} and morphologies ranging from a normal spiral to merging galaxies.

In this work we extend to higher redshifts the comparison between different SFR estimators that have been used for samples of local galaxies (e.g., Sullivan et al. 2001). For that purpose, we compare classical SFR indicators such as the nebular emission lines [O II] and Hα, or the UV continuum, which we correct for dust extinction using the Balmer decrement, with the FIR and radio luminosities, which are unaffected by extinction. This has been made possible with the commissioning of high-resolution optical and near-infrared (NIR) spectroscopy on the Keck telescopes. High-resolution spectroscopy is required not only to avoid the contamination from atmospheric OH emission lines but also to resolve the [N II] $\lambda\lambda$6549, 6583 and Hα emission lines. After the presentation of the observational data in § 2, the fluxes in these three lines will be combined in § 3 with the [O III] and Hβ lines to locate galaxies in diagnostic diagrams that allow separating galaxies whose optical luminosity is mainly due to star formation from galaxies where an active galactic nucleus (AGN) is the dominant source of emission.

In § 4 we obtain multiwavelength SFR estimates for the galaxy sample using the available flux data. Additional galaxy parameters are examined in § 5, and a summary of the main properties of each object is presented in § 6. In § 7 we compare and discuss the results obtained using the different SFR estimators. Finally, we present the conclusions in § 8.

Unless otherwise indicated, throughout this paper we will assume $H_0 = 70$ km s^{-1} Mpc^{-1}, $\Omega_M = 0.3$, and $\Omega_\Lambda = 0.7$.

2. THE DATA

2.1. *Galaxy Sample and Observations*

The sample of dusty starburst galaxies was chosen according to the availability of ISOCAM 15 μm luminosities (or, at least, upper limits) for each object. The galaxies were also constrained to have a spectroscopic redshift accurate enough to ensure that the Hα line would be free of contamination as a result of night-sky lines. With those criteria in mind, we have selected four galaxies with a mean redshift $\langle z \rangle \sim 0.46$ in the Hubble Deep Field–North (HDF-N; Williams et al. 1996) and three galaxies with $\langle z \rangle \sim 0.80$ in the Groth Strip Survey (GSS; Groth et al. 1994; Koo et al. 1996). The whole set of galaxies is listed in Table 1 and displayed in Figure 1. Interestingly, the two galaxies undetected by *ISO* have a compact morphology (hd2-264.2 and GSS 084_4515). The *ISO* sources are face-on spirals (hd4-656.1, hd4-795.111, and GSS 084_4521), a disky galaxy (hd2-264.1), and a colliding system (GSS 073_1810) that looks like a higher redshift analog of the local Antennae system (NGC 4038 and NGC 4039). In order to facilitate the recognition of the individual objects in some of the figures of this paper, we have labeled the symbols with the letters S, D, C, and A, corresponding to their morphologies, i.e., spiral, disky, compact, and Antennae-like, respectively.

According to their IR luminosities (computed as described in § 4.3), the HDF-N galaxies are not luminous enough to be classified as luminous infrared galaxies (LIRGs; $L_{\mathrm{IR}} \geq 10^{11}$ $L_\odot$), whereas the contrary is true for the GSS objects. Note that although GSS 073_1810 could be marginally considered as an ultraluminous infrared galaxy (ULIRG; $L_{\mathrm{IR}} \geq 10^{12}$ $L_\odot$), this object is constituted by two colliding galaxies (see Fig. 1). A more detailed characterization of the galaxy sample is presented in §§ 5 and 6.

For all galaxies in our sample, we have obtained optical and NIR spectroscopy. The observations were carried out with the W. M. Keck Observatory telescopes and three different instruments over five observing runs (see Table 1). For the relatively low redshift HDF-N galaxies, we employed the Echelle Spectrograph and Imager (ESI; Sutin 1997; Epps & Miller 1998; Sheinis et al. 2002), which covers the full wavelength range from 3900 to 11000 Å in one configuration, with a spectral resolution FWHM ~ 0.8 Å at observed $\lambda(\mathrm{H}\alpha) \sim 9600$ Å. However, for the more distant GSS galaxies, initially only observed in the spectral range 4500–9000 Å with the Low Resolution Imaging Spectrometer (LRIS; Oke et al. 1995; FWHM ~ 3 Å), we expanded the spectral window by using the NIR echelle spectrograph NIRSPEC (McLean et al. 1998) in the J band (N2 and N3 filters, total spectral range 1.089–1.375 μm, FWHM ~ 8 Å).

TABLE 1
Galaxy Sample

Galaxy[a]	R.A.[b]	Decl.[b]	z_{spec}[c]	$E_G(B-V)$[d]	Run[e]	t_{exp}[f] (s)
hd2-264.1	12 36 49.76	62 13 13.1	0.475	0.012	4 (0.75)	1200
hd2-264.2	12 36 49.38	62 13 11.2	0.477	0.012	4 (0.75)	1200
hd4-656.1	12 36 42.91	62 12 16.3	0.454	0.012	4 (1.25)	900
hd4-795.111	12 36 41.95	62 12 05.4	0.433	0.012	4 (1.25)	900
GSS 073_1810	14 17 42.64	52 28 45.3	0.831	0.007	1 (1.18), 5 (0.76)	3000, 2400
GSS 084_4515	14 17 40.43	52 27 19.4	0.812	0.008	3 (1.00), 5 (0.76)	3600, 2400
GSS 084_4521	14 17 40.55	52 27 13.6	0.754	0.008	2 (1.00), 5 (0.76)	3000, 2400

Note.—Units of right ascension are hours, minutes, and seconds, and units of declination are degrees, arcminutes, and arcseconds.

[a] Galaxy identification: for the HDF galaxies we follow Williams et al. 1996, whereas for the GSS galaxies we employ a name based on the field and the WFPC chip numbers, as well as the first two digits of the X and Y centroid coordinates.

[b] J2000.0 coordinates for the HDF (drizzled Version 2) and GSS (Rhodes et al. 1994) galaxies.

[c] Spectroscopic redshifts obtained from measurements of individual spectral features and/or cross-correlation technique.

[d] Galactic color excesses derived from the dust maps of Schlegel et al. 1998 and the software available at http://astron.berkeley.edu/davis/dust.

[e] Spectroscopic observing runs with Keck: 1=LRIS (1996 April), 2=LRIS (1997 May), 3=LRIS (1998 April), 4=ESI (2000 May), and 5=NIRSPEC (2000 July). Slit widths (in arcseconds) employed in each case are given in parentheses.

[f] Total exposure times.

In general, the observations were carried out with air masses ranging from 1.09 to 1.56.

2.2. *Data Reduction and Error Handling*

The reduction of the LRIS data (runs 1, 2, and 3) is as described in Simard et al. (1999). The absolute flux calibration used observations of the spectrophotometric standard BD $+33^\circ2642$ (runs 1 and 3) as the primary calibrator and the spectra of two stars, GSS 063_0445 and GSS 093_2453 (runs 1, 2, and 3), used to align the image masks, as secondary calibrators. We find that the response curve of LRIS is very stable on a run-to-run basis, with small fluctuations $\lesssim 5\%$, which translate into negligible variations in the SFRs once other sources of error and uncertainties are considered.

The ESI (run 4) and NIRSPEC (run 5) spectra have been reduced using a suite of our own programs based on the REDUCEME package (Cardiel 1999) and a new FORTRAN package, XNIRSPEC, specially developed for the reduction of the NIR data. Error frames have been computed directly from the raw images, using the readout noise and the gain of each detector. The reduction in parallel of these error frames together with the data images guarantees the correct propagation of errors due to arithmetic manipulation throughout the reduction procedure (Cardiel et al. 1998, 2003). In this sense, each fully processed spectrum is accompanied by an associated error spectrum that contains the random error in each pixel due to photon statistics and readout noise.

One of the major problems encountered when measuring spectral features in the NIR is the proper removal of the OH emission lines (Rousselot et al. 2000) and the compensation for telluric absorption due to water vapor and other molecules (Stevenson 1994; Chmielewski 2000). Systematic variations in the spectral direction (e.g., sampling aliasing, inaccurate geometric distortion corrections) and in flux calibration (e.g., even small flat-field biases, residual fringing, or slit width inhomogeneities) pose a difficult challenge to the data reduction. Trying to minimize part of these problems, the NIRSPEC observations were carried out nodding the telescope, changing the position of the galaxies on the slit, in order to feed the data reduction pipeline with the subtraction of consecutive images. Even when following this procedure, the unpredictable residuals of each sky line (either in intensity or sign) had to be subtracted like normal sky lines in a subsequent step.

Since the spectra obtained in the detector plane of ESI and NIRSPEC are distorted, the image rectification prior to the removal of sky lines generates aliasing artifacts (the undersampled sky line residuals cannot be properly rectified) and, in addition, introduces a correlation between adjacent pixels in the error frames. In order to alleviate both effects, we mapped the image distortions in the spatial and spectral directions by using bivariate polynomial transformations (Wolberg 1990). These mapping functions were determined by fitting the spectrum of a bright star, observed at different positions along the slit, and to the sky lines.

For the ESI observations, the removal of the telluric absorption, as well as the absolute flux calibration, used the high signal-to-noise ratio (S/N per Å $\gtrsim 150$), almost featureless spectra of the spectrophotometric stars (BD $+28^\circ4211$, Wolf 1346, and Feige 34). In the NIRSPEC run only one spectrophotometric star was observed (BD $+28^\circ4211$), and the removal of telluric features was performed using the observation of V986 Oph, a hot (B0 III) and bright ($V = 6.15$ mag) star.

All the flux-calibrated spectra are displayed in Figures 2 and 3.

2.3. *Measure of Emission-Line Fluxes*

The spectra have been corrected for atmospheric extinction using the Mauna Kea values available on the Web site of the United Kingdom Infrared Telescope (UKIRT). The small corrections for Galactic extinction used the dust maps of Schlegel, Finkbeiner, & Davis (1998) and the Galactic extinction curve of Fitzpatrick (1999).

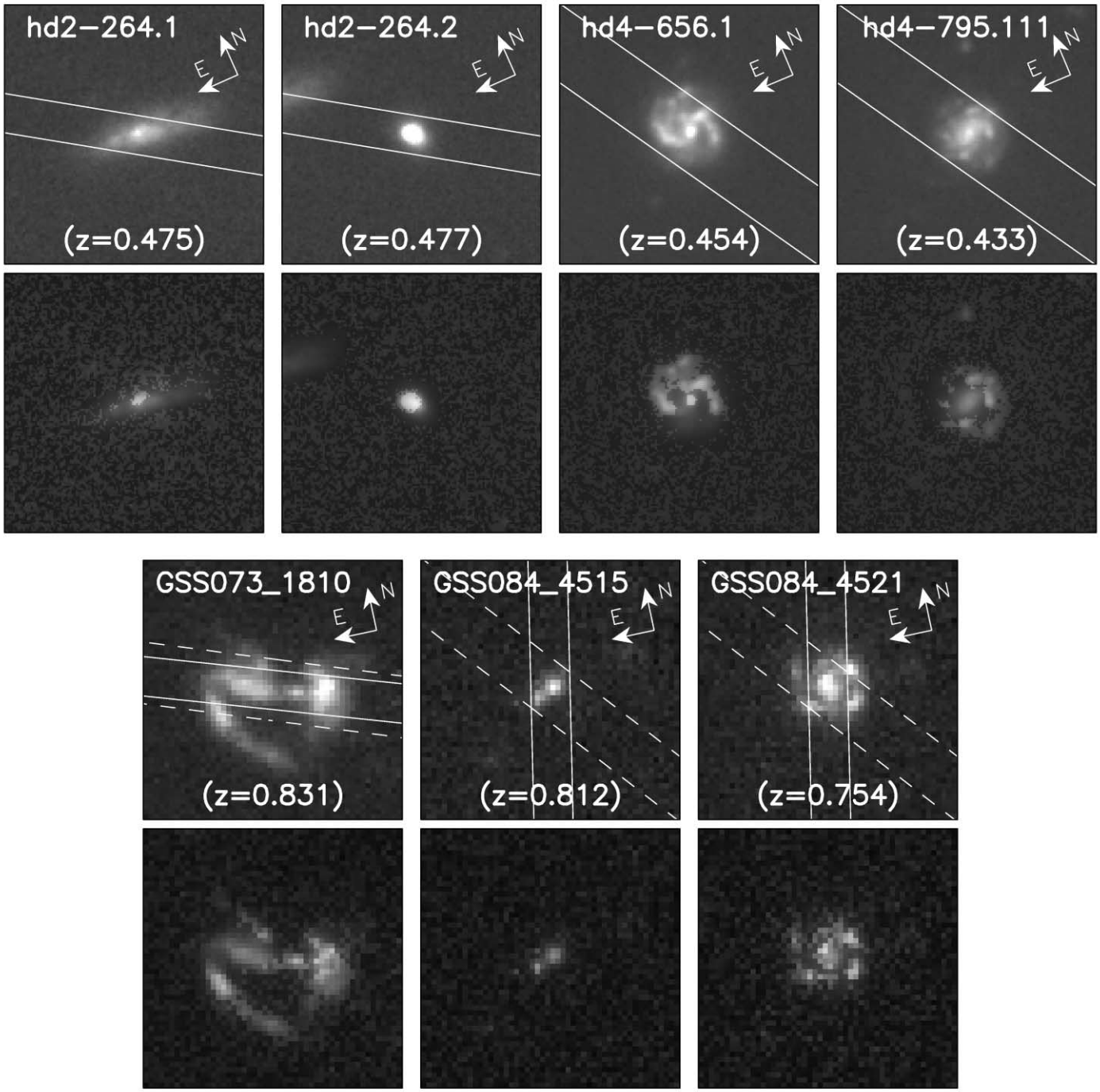

FIG. 1.—*HST* images of the whole galaxy sample. Each panel corresponds to $5'' \times 5''$. The upper panel of each object is a composite *RGB* image derived from the combination of the flux-calibrated images. For the HDF-N galaxies, the average of F300W and F450W was employed as *B*, F606W as *G*, and F814W as *R*. For the GSS galaxies only F606W and F814W were available. For that reason, the former was employed as *B*, the latter as *R*, and the average of both as *G*. The lower panels are blue and red enhanced compositions, in which the reddest and bluest regions have been intentionally exaggerated. For that purpose, all the images for each galaxy were scaled to the same total averaged flux *per unit wavelength* prior to the color composition (in this sense, differential color variations are easier to display). Next, images were assigned to *RGB* using the same criterion as with the upper panels, but before combining them, the weighting factors $(1, \frac{1}{2}, \frac{1}{4})$ and $(\frac{1}{4}, \frac{1}{2}, 1)$ were applied to the (R, G, B) set of each pixel, which held $R > B$ and $R < B$, respectively. For the HDF-N galaxies the solid lines indicate the orientation and width of the slit in the observation with ESI. For the GSS galaxies the solid and dashed lines correspond to the slit employed in the observation with NIRSPEC and LRIS, respectively. We remind the readers that total exposure times for HDF-N images are 153,700 (F300W), 120,600 (F450W), 109,050 (F606W), and 123,600 s (F814W). For GSS 073 these numbers are 24,400 (F606W) and 25,200 s (F814W), whereas the integrations in GSS 084 are the shortest, 2800 (F606W) and 4400 s (F814W). [*See the electronic edition of the Journal for a color version of this figure.*]

With the aim of correcting the measured Balmer emission line fluxes for the expected underlying stellar absorption, we have applied the criterion followed by Calzetti, Kinney, & Storchi-Bergmann (1994), who, based on the extensive analysis of giant extragalactic H II regions by McCall, Rybski, & Shields (1985), employed $\mathrm{EW}_{\mathrm{abs}}(\mathrm{H}\alpha) = \mathrm{EW}_{\mathrm{abs}}(\mathrm{H}\beta) = 2$ Å for galaxies with undetected or uncertain Hγ flux.

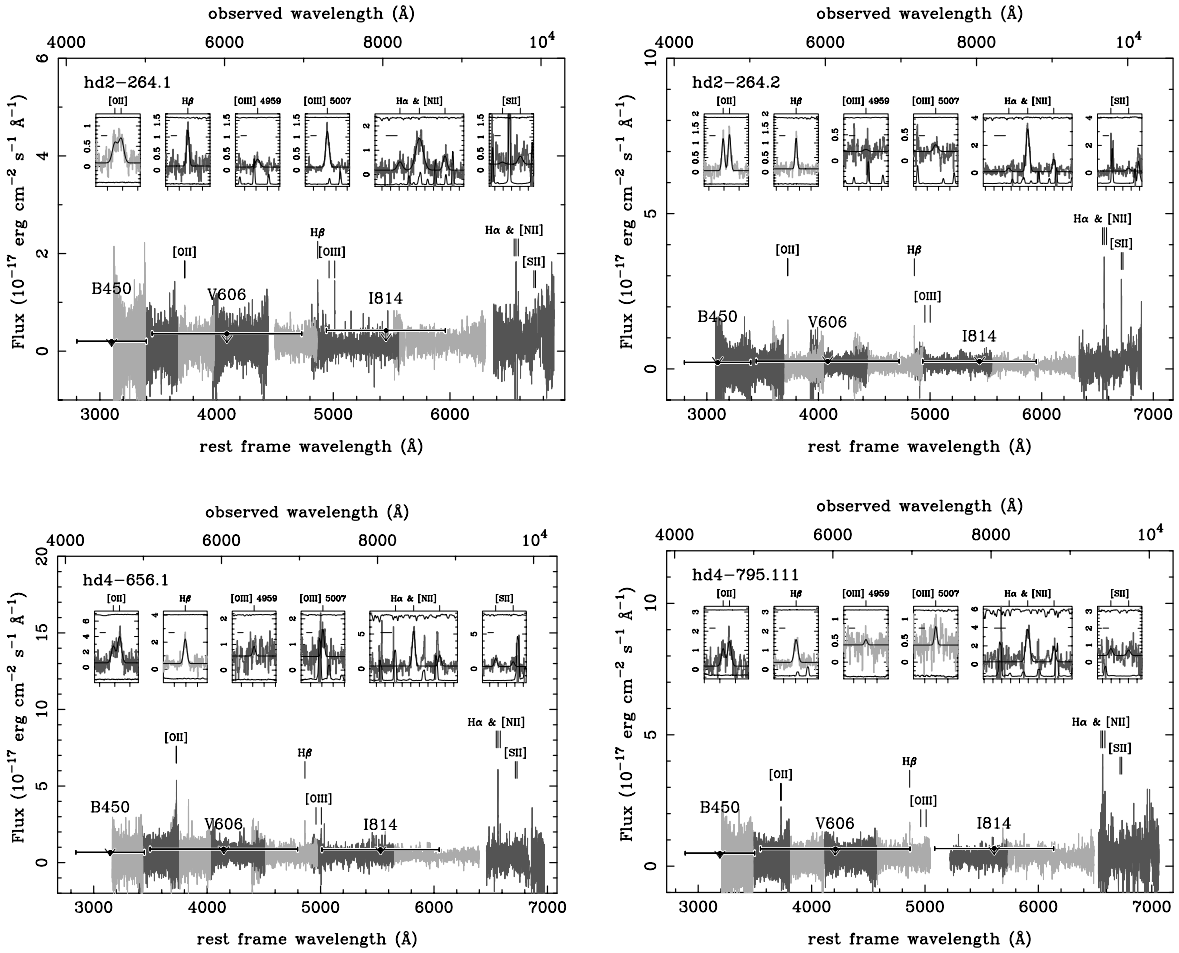

FIG. 2.—Flux-calibrated spectra for the HDF-N galaxy subsample. Each gray-scale intensity identifies a different order in the ESI echelle spectra. Very high sky residuals have been masked only for display purposes. The location of the detected emission lines is marked. The insets show the fits to each emission line (in these enlargements sky residuals have not been masked). Inside these panels we have also plotted the normalized atmospheric transmission (*upper curve*, with the zero level marked by the short horizontal line in the upper left side), the subtracted sky spectrum (*lower curve*, in arbitrary units), and the resulting emission-line fit (*thin line overplotted on spectrum*). The zoomed wavelength range is 1600 km s^{-1} (3200 km s^{-1} for the "Hα & [N II]" panel), with ticks every 10 Å (observed wavelength). The broadband photometry collected in Table 4 is also displayed. Error bars in the spectral direction represent the filter coverage, whereas the arrows indicate the decrease in flux after applying the aperture corrections given in Table 3. There is a good agreement in the absolute flux calibration of the spectroscopic and broadband photometry data. The residual fringing present in the ESI data is responsible for the high residuals in the Hα and [S II] regions.

In order to follow a homogeneous procedure in the determination of line luminosities, line fluxes have been derived from Gaussian fits to the corresponding emission lines. It is worth noting that these fits not only match the observed spectra within the error bars available in each pixel, but they also help minimize the uncertainties due to the choice of integration limits on both sides of the emission lines. Flux errors are also easily computed in this way through numerical simulations with bootstrapped error spectra. All the measured emission lines are displayed in the insets of Figures 2 and 3 (see caption for details). Their values are listed in Table 2. Considering that the Hα line has been observed in spectral regions densely populated by sky lines, it is not surprising that in some cases large residuals prevented fitting Gaussians to the entire wavelength domain of the [N II] λλ6549, 6583 lines. In these cases (and also when no clear signature of these lines was detectable), since the expected location of the lines is very well constrained by the centroid of the Hα line, restricted fits were performed to the line regions free of contamination (see note of Table 2 for details). Restricted fits have also been applied to other emission lines when required.

Intrinsic reddenings, parameterized through the color excess in the nebular gas, $E(B-V)_{\rm gas}$, were determined using the measured Balmer decrement and assuming typical gas conditions, i.e., $N_e = 10^2$ cm^{-3}, $T_e = 10^4$ K, recombination case B, and the flux ratio $\mathrm{H}\alpha/\mathrm{H}\beta = 2.86$ (Osterbrock 1989). Since the extinction properties of the Milky Way (Savage & Mathis 1979; Seaton 1979; Cardelli, Clayton, & Mathis 1989; O'Donnell 1994; Fitzpatrick 1999), the Small Magellanic Cloud (Prévot et al. 1984; Bouchet et al. 1985), and the Large Magellanic Cloud (Howarth 1983; Fitzpatrick 1985) are similar in the optical and in the NIR spectral ranges, it is common to assume that the selective extinction curve from any of these objects can be safely used to correct the emission lines for internal reddening (Calzetti 1997). For this reason, here we adopt the average curve for Galactic extinction published by Fitzpatrick (1999). The $E(B-V)_{\rm gas}$ values for our galaxy sample are given in the last column

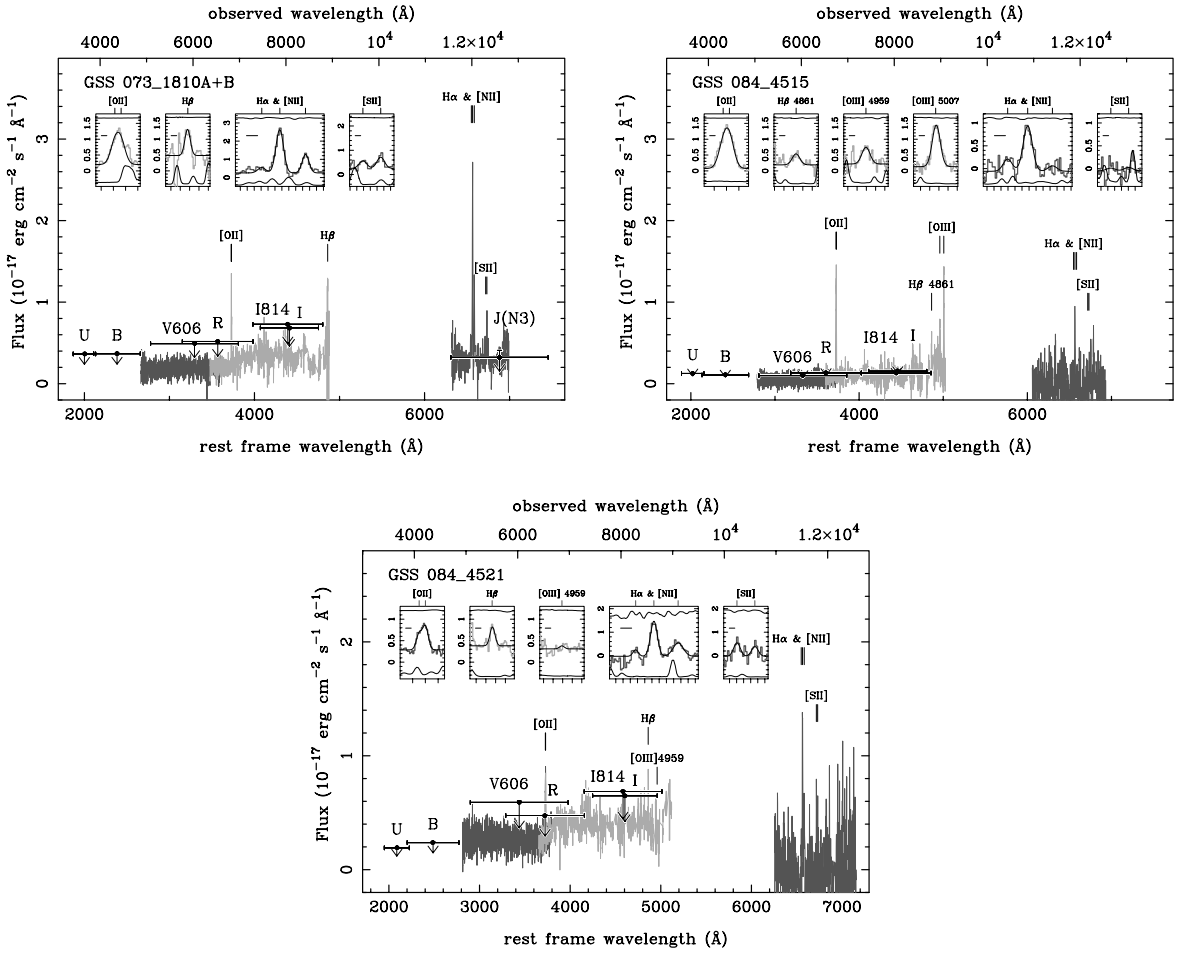

FIG. 3.—Flux-calibrated spectra for the GSS galaxy subsample. In this case, LRIS spectra are plotted together with NIRSPEC data. See caption of Fig. 2 for explanation. The broadband photometry corresponds to data collected in Table 5. Note that for these objects, the agreement in the absolute flux calibration of the spectroscopic and broadband photometry data is also good, except for the J_{N3} value of GSS 073_1810. However, in this case the uncertainty is much larger than in the rest of the broadband measurements (note that we have plotted an upper error bar segment in flux for this point).

of Table 2. The quoted errors correspond to the propagation of random errors in the Hα and Hβ fluxes.

Finally, to estimate the impact of the slit widths and position angles in the measured emission-line fluxes, we computed the fraction of light passing through the slit for each observation, using the *HST* images; these fractions and associated errors are listed in Table 3. The errors were calculated using numerical simulations that assume random positioning errors when placing the slits over the targets. The simulations were performed after isolating each galaxy from its neighbors using SExtractor (Bertin & Arnouts 1996), with the configuration parameter CHECKIMAGE_TYPE set to OBJECTS. Although those slit-loss estimates must be taken with caution, it seems unlikely that we are losing more than 50% of the light in any case.

2.4. *Additional Flux Data*

Additional photometric data, shown in Tables 4, 5, and 6, were used as consistency checks on the absolute flux calibration over the entire wavelength range. These data were also used to estimate the importance of the aperture correction when measuring the emission-line fluxes (see Figs. 2 and 3) and to derive SFRs based on UV, IR, and radio luminosities.

The *HST* magnitudes for the HDF-N galaxies (Table 4) correspond to the fluxes published by Fernández-Soto, Lanzetta, & Yahil (1999).

For the GSS galaxies (Table 5) we list the *U*-, *B*-, *R*-, and *I*-band magnitudes determined by Brunner, Connolly, & Szalay (1999) using photometric data obtained with the Prime Focus CCD (PFCCD) camera on the Mayall 4 m telescope at Kitt Peak National Observatory (KPNO). In addition, we have computed V_{606} and I_{814} magnitudes using SExtractor (Bertin & Arnouts 1996) applied on the *HST* images (Groth et al. 1994). We have also compared the KPNO magnitudes with their analogous *HST* measurements. In this sense, a small offset of 0.15 mag has been detected between the KPNO *I*-band magnitudes and the *HST* I_{814} data (see Fig. 4). We do not make a similar correction for the KPNO *R*-band magnitudes because the overlap in wavelength with the V_{606} bandpass is small and the comparison between both magnitudes has a large scatter. Finally, we also derived a direct measurement of the *J*-band magnitude for the pair of interacting galaxies GSS 073_1810. In this case, we made use of the images obtained with the slit-viewing camera SCAM of NIRSPEC through the N3 filter (covering the range 1.143–1.375 μm). Although the total effective exposure time only lasted 80 s, it was enough to get

TABLE 2

MEASURED EMISSION-LINE FLUXES AND COLOR EXCESSES

Galaxy	F([O II]) $\lambda\lambda$3727, 3729	F(Hβ) λ4861	F([O III]) λ4959	F([O III]) λ5007	F([N II]) λ6549	F(Hα) λ6563	F([N II]) λ6583	F([S II]) λ6717	F([S II]) λ6734	$E(B-V)_{\rm gas}$
hd2-264.1	4.49 (2)	3.33 (1)	1.11 (1)	3.99 (1)	2.46 (1)	14.7 (1)	3.23 (1)	0.40 (3)	1.62 (3)	$0.37^{+0.15}_{-0.14}$
	0.55	0.44	0.72	0.22	2.13	1.4	0.72	0.41	0.98	
hd2-264.2	4.98 (2)	2.72 (1)	0.21 (3)	>0.63 (1)	1.27 (3)	15.0 (1)	3.61 (1)	...	1.00 (3)	$0.56^{+0.10}_{-0.09}$
	0.25	0.25	0.23	...	0.58	0.7	0.69	...	0.50	
hd4-656.1	17.9 (2)	7.46 (1)	1.11 (3)	3.11 (3)	...	22.7 (1)	6.18 (3)	4.60 (3)	2.70 (3)	$0.04^{+0.05}_{-0.04}$
	0.9	0.30	0.61	1.57	...	0.9	1.60	1.19	0.77	
hd4-795.111	6.29 (2)	5.58 (1)	0.35 (3)	1.21 (1)	...	20.4 (1)	6.59 (1)	1.98 (3)	1.57 (3)	$0.20^{+0.07}_{-0.06}$
	0.55	0.29	0.16	0.35	...	1.1	1.34	0.53	0.42	
GSS 073_1810A	7.46 (2)	4.61 (1)	...	...	2.98 (3)	22.3 (1)	8.37 (1)	2.83 (3)	4.70 (3)	$0.45^{+0.12}_{-0.11}$
	0.10	0.52	...	...	0.68	1.3	1.28	0.48	0.78	
GSS 073_1810B	3.87 (2)	2.92 (1)	...	...	1.65 (3)	11.2 (1)	4.88 (1)	1.73 (3)	2.03 (1)	$0.24^{+0.18}_{-0.16}$
	0.10	0.48	...	...	0.63	1.1	0.90	0.38	0.83	
GSS 084_4515	16.4 (2)	4.35 (1)	6.18 (1)	15.3 (1)	4.20 (3)	16.2 (1)	1.83 (3)	1.00 (3)	1.20 (3)	$0.22^{+0.17}_{-0.17}$
	0.2	0.62	0.76	0.5	1.75	2.2	1.20	1.32	1.55	
GSS 084_4521	5.05 (2)	3.82 (3)	0.38 (3)	...	2.53 (1)	17.6 (1)	10.1 (1)	5.77 (3)	4.30 (3)	$0.41^{+0.35}_{-0.27}$
	0.09	1.24	0.28	...	1.88	1.9	4.9	3.08	2.35	

NOTE.—Total measured (i.e., uncorrected for intrinsic reddening) emission-line fluxes, in units of 10^{-17} ergs s^{-1} cm^{-2}. Random errors are given below each flux value. Numbers in parentheses indicate the type of Gaussian fit performed to the emission lines: (1) Gaussian with three free parameters; (2) two Gaussians with the same width, different amplitude, and fixed separation; (3) Gaussian with fixed width and position. In the case of the restricted fits (types 2 and 3), the a priori required fixed values have been taken from neighbor and similar lines. [O III] lines for GSS 073_1810 are outside the observed spectral range. The remaining void entries in the table are due to very high sky line residuals. Note that these numbers have not been corrected for aperture effects.

TABLE 3
APERTURE CORRECTIONS ESTIMATES

Galaxy	U_{300} Slit 0.″75	B_{450} Slit 0.″75	V_{606} Slit 0.″75	I_{814} Slit 0.″75
hd2-264.1	0.61 (0.52 ± 0.11)	0.58 (0.50 ± 0.12)	0.58 (0.50 ± 0.12)	0.60 (0.51 ± 0.11)
hd2-264.2	0.96 (0.75 ± 0.30)	0.92 (0.72 ± 0.27)	0.90 (0.70 ± 0.26)	0.88 (0.66 ± 0.27)
	U_{300} Slit 1.″25	B_{450} Slit 1.″25	V_{606} Slit 1.″25	I_{814} Slit 1.″25
hd4-656.1	0.85 (0.69 ± 0.17)	0.84 (0.67 ± 0.18)	0.82 (0.67 ± 0.17)	0.81 (0.68 ± 0.15)
hd4-795.111	0.77 (0.63 ± 0.14)	0.78 (0.62 ± 0.17)	0.81 (0.65 ± 0.17)	0.86 (0.68 ± 0.17)
	V_{606} Slit 0.″76	I_{814} Slit 0.″76	V_{606} Slit 1.″18	I_{814} Slit 1.″18
GSS 073_1810	0.52 (0.45 ± 0.10)	0.56 (0.47 ± 0.11)	0.69 (0.65 ± 0.06)	0.72 (0.67 ± 0.07)
	V_{606} Slit 0.″76	I_{814} Slit 0.″76	V_{606} Slit 1.″00	I_{814} Slit 1.″00
GSS 084_4515	0.88 (0.60 ± 0.24)	0.90 (0.67 ± 0.25)	0.94 (0.76 ± 0.22)	0.97 (0.81 ± 0.21)
GSS 084_4521	0.60 (0.50 ± 0.10)	0.61 (0.52 ± 0.11)	0.73 (0.62 ± 0.14)	0.74 (0.65 ± 0.12)

NOTE.—Fraction of light inside the slit for all the observational configurations. These numbers have been measured in the available *HST* images (F300W, F450W, F606W, and F814W for HDF-N galaxies; F606W and F814W for GSS galaxies). The numbers in parentheses indicate the mean and standard deviation in numerical simulations, assuming typical errors in the positioning of the slit on the targets of 0.″1 in both right ascension and declination and of 3° in position angle.

the absolute flux with a relative random uncertainty of ~25%.

The MIR flux densities (Table 6), $S_\nu(15\ \mu\mathrm{m})$, are the ISOCAM measurements with the LW3 filter published by Aussel et al. (1999) and Flores et al. (1999) for the HDF-N and the GSS galaxies, respectively. Nondetections are indicated by an upper limit, which corresponds to the sensitivity threshold of the surveys. The flux published by Aussel et al. (1999) for hd2-264.1 integrates the emission of four blended sources. The flux value given here is the result for only this galaxy, obtained after deconvolving the different objects (H. Aussel 2001, private communication). The fluxes for GSS 073_1810 and GSS 084_4521 are also revised values (after improving the flux calibration through Monte Carlo simulations; H. Flores 2001, private communication).

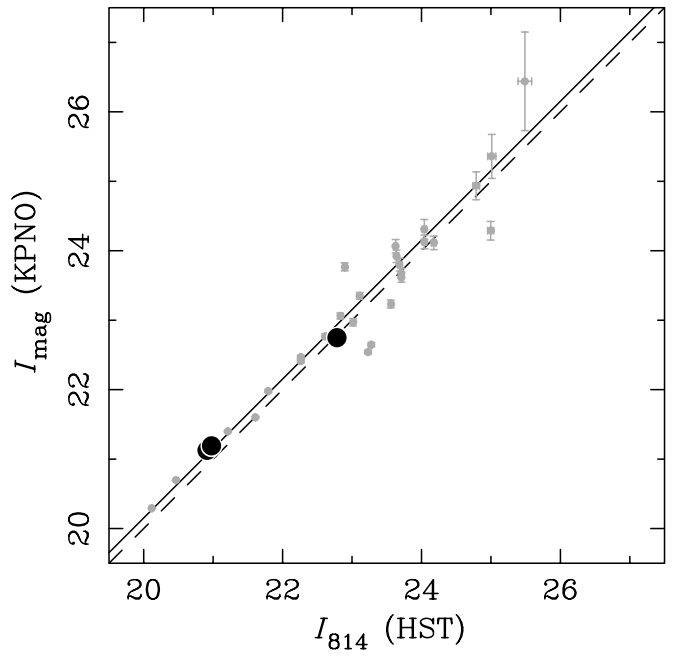

FIG. 4.—Comparison of the KPNO I_{mag} with *HST* I_{814} magnitudes (AB system). The data correspond to measurements of objects in GSS 073 (the GSS field with the largest exposure times; see caption of Fig. 1). KPNO magnitudes come from Brunner et al. (1999). *HST* magnitudes have been measured in this work with SExtractor (Bertin & Arnouts 1996). The three GSS galaxies of our sample are plotted as big circles. The dashed line is the 1 : 1 relation, whereas the solid line is the weighted least-squares fit to a straight line of slope unity. The offset between both lines is 0.15 mag.

The radio flux densities (last column in Table 6), S_ν(radio), are the 8.5 GHz measurements from Richards et al. (1998) for the HDF-N galaxies and the 5.0 GHz data from Fomalont et al. (1991) for the GSS objects. We also quote the sensitivity limit of the considered survey for the undetected galaxies. Finally, to be consistent with the estimation of the MIR flux for hd2-264.1, we consider that the radio flux in this case also integrates the combined values of the blended sources. Thus, the quoted radio flux is the same fraction of the total radio flux.

3. CONSTRAINING THE AGN CONTRIBUTION

Before calculating the SFRs from the collected multiwavelength data, we must consider the possible contamination of our galaxy sample by AGNs. The fact that QSOs and ULIRGs exhibit similar total luminosities and space densities led Sanders et al. (1988) to suggest that ULIRGs may constitute the dust-enshrouded phase of QSO formation. In this sense, strong interactions and mergers are the mechanisms responsible for the funneling of gas into the central regions of galaxies, which subsequently may feed both star formation and AGN activity. Although some aspects of this scenario are still controversial, observations confirm the connection between QSOs, ULIRGs, and mergers (Canalizo & Stockton 2001 and references therein). In

TABLE 4
ADDITIONAL FLUX DATA FOR HDF-N GALAXIES

Galaxy	U_{300}[a]	B_{450}[a]	V_{606}[a]	I_{814}[a]	K[a]
hd2-264.1	24.93 ± 0.08	23.52 ± 0.01	22.30 ± 0.01	21.50 ± 0.01	19.93 ± 0.01
hd2-264.2	24.12 ± 0.03	23.48 ± 0.01	22.70 ± 0.01	22.10 ± 0.01	21.43 ± 0.02
hd4-656.1	22.84 ± 0.01	22.22 ± 0.01	21.33 ± 0.01	20.74 ± 0.01	19.91 ± 0.01
hd4-795.111	23.22 ± 0.02	22.55 ± 0.01	21.64 ± 0.01	21.00 ± 0.01	19.92 ± 0.01

[a] Magnitudes are given in the AB system, where $m = -2.5 \log f_\nu - 48.60$, with f_ν in ergs cm^{-2} s^{-1} Hz^{-1}. All the data are extracted from Table 5 of Fernández-Soto et al. 1999.

conclusion, rather than segregating LIRGs and ULIRGs into starbursts and AGNs, the key factor is to constrain the relative contribution of each component to the IR luminosity in a case-by-case basis.

3.1. *Emission-Line Diagnostic Diagrams*

An important constraint on the contribution of AGN radiation, if any, to the total luminosity of our galaxies comes from the use of emission-line diagnostic diagrams. The set of emission lines displayed in Table 2 allows us to examine two of the most commonly employed diagrams. In Figure 5 we compare the ratio [O III] $\lambda5007/\mathrm{H}\beta$ (which is an indicator of the gas excitation) versus the ratios [N II] $\lambda6583/\mathrm{H}\alpha$ and [S II] $\lambda\lambda6716, 6731/\mathrm{H}\alpha$ (the tabulated line ratios are also given in Table 7). Two interesting properties of these diagrams are their ability to properly discriminate between mechanisms responsible for the gas ionization (star formation, AGNs, or shocks) and their low sensitivity to extinction corrections. The latter is clearly manifest in our data, since the mean correction of the plotted ratios in our galaxy sample is only 2%, with a maximum of 7% for the [O III] $\lambda5007/\mathrm{H}\beta$ ratio in hd2-264.2. In Figures 5*a* and 5*b* we display a large collection of emission-line ratios corresponding to nearby galaxies from Veilleux & Osterbrock (1987, hereafter VO87) and Gallego et al. (1996; see table caption for details), whereas in Figures 5*c* and 5*d* we do the same with our galaxy sample. The analysis of this figure clearly indicates that the locus spanned by our galaxies is perfectly compatible with that exhibited by star-forming galaxies.

It is also very interesting to compare the measured line fluxes exhibited by our galaxy sample, in particular the ratio [O III] $\lambda5007/\mathrm{H}\beta$ (an indicator of the emitting gas excitation), with those of local star-forming galaxies, as a function of luminosity. For this purpose, we have estimated rest-frame absolute blue magnitudes for each galaxy using the available *HST* V_{606} and I_{814} magnitudes (note that the *HST* F606W and F814W bandpasses correspond approximately to the rest-frame *B* band at $z \sim 0.4$ and 0.8, which are precisely quite close to the redshifts exhibited by the present sample). The *HST* fluxes were corrected for redshift, the transmission curves of filters F606W and F814W were deredshifted to reproduce pseudo-*B* bands for each target, and a residual *k*-correction (ranging from -0.06 to 0.28 mag) was derived for each object, using the averaged spectral energy distributions (SEDs) corresponding to Sab, Sbc, and Scd galaxies of Fukugita, Shimasaku, & Ichikawa (1995). The resulting magnitudes are listed in Table 8, and the excitation diagram is displayed in Figure 6. For comparison, we have included in the same figure the very well characterized local sample of the UCM survey (Gallego et al. 1996, 1997), using different symbols to discriminate among distinct star-forming galaxies: SBNs (starburst nuclei; originally defined by Balzano 1983) are spiral galaxies that host a nucleus with an important star-forming process, with Hα luminosities always higher than 10^8 $L_\odot$; DANSs (dwarf amorphous nucleus starbursts; introduced by Salzer, McAlpine, & Boroson 1989) are similar to SBNs but at lower scale; HIIHs (H II galaxy hot spots; see Gallego et al. 1996) are bright galaxies with a global star-forming process, optical spectrum dominated by blue colors, and strong emission lines; they show similar Hα luminosities to those exhibited by SBNs, but with large [O III]/Hβ ratios; DHIIHs (dwarf H II hot spots) are similar to HIIHs, but with Hα luminosities lower than 5×10^7 $L_\odot$; and BCDs (blue compact dwarfs) are star-forming galaxies with the lowest luminosity and higher ionization. Finally, Seyfert 2 galaxies (Sy2) are also displayed in Figure 6 to show the plot region covered by AGN-dominated objects. The analysis of this figure reveals that the galaxies of our sample are perfectly compatible with the locus of local SBNs, with the exception of hd2-264.2, which, based on its higher [O III]/Hβ ratio, is located in the region of local HIIH objects.

TABLE 5
ADDITIONAL FLUX DATA FOR GSS GALAXIES

Galaxy	U_{mag}[a]	B_{mag}[a]	R_{mag}[a]	I_{mag}[a,b]	V_{606}[c]	I_{814}[c]	J_{N3}[d]
GSS 073_1810[e]	23.38 ± 0.02	23.00 ± 0.02	21.76 ± 0.01	20.98 ± 0.01	22.00 ± 0.01	20.91 ± 0.01	20.83 ± 0.28
GSS 084_4515	24.54 ± 0.04	24.34 ± 0.04	23.24 ± 0.03	22.60 ± 0.04	23.73 ± 0.04	22.78 ± 0.02	...
GSS 084_4521	24.08 ± 0.02	23.47 ± 0.02	21.85 ± 0.01	21.04 ± 0.01	21.80 ± 0.02	20.98 ± 0.01	...

[a] Magnitudes are given in the AB system, where $m = -2.5 \log f_\nu - 48.60$, with f_ν in ergs cm^{-2} s^{-1} Hz^{-1}. Data are extracted from Brunner et al. 1999.
[b] The I_{mag} values have been corrected for the 0.15 mag offset found in the comparison shown in Fig. 4.
[c] *HST* V_{606} and I_{814} magnitudes in the AB system, measured in this work using SExtractor (Bertin & Arnouts 1996).
[d] NIRSPEC *J* magnitude (filter N3) measured in this work (see text for details).
[e] Tabulated magnitudes correspond to the integrated values of the two interacting galaxies.

TABLE 6

MIR and Radio Fluxes for the Galaxy Sample

Galaxy	$S_\nu(15\ \mu\mathrm{m})$[a] (μJy)	$S_\nu(\mathrm{radio})$[b] (μJy)
hd2-264.1	115 ± 40	14 ± 3
hd2-264.2	<100	<9
hd4-656.1	49^{+36}_{-9}	<9
hd4-795.111	52^{+34}_{-9}	<9
GSS 073_1810[c]	361 ± 80	$\lesssim 16$
GSS 084_4515	<200	<16
GSS 084_4521	240 ± 90	24 ± 4

[a] MIR flux densities, as measured by ISOCAM with the LW3 filter. See references in the text.

[b] Radio flux densities, at 8.5 GHz for the HDF-N galaxies and at 5.0 GHz for the GSS galaxies. See references in the text.

[c] Tabulated fluxes correspond to the integrated values of the two interacting galaxies.

3.2. *Further Evidence*

There is a growing body of evidence indicating that the population of IR luminous galaxies detected by the ISOCAM deep surveys is composed of generally dust-obscured starbursts (Fadda et al. 2002; Elbaz et al. 2002). Genzel et al. (1998) and Laurent et al. (2000) report the presence of a dichotomy in the spectroscopic properties of starbursts and galaxies whose luminosity is dominated by gravitational accretion: the former show stronger MIR broad emission features, with a fast decline in their emission shortward of $\lambda \sim 6\ \mu$m, whereas AGNs are characterized by a flatter spectrum. Through the analysis of these features, Tran et al. (2001) showed that AGN activity is dominant in local ULIRGs only for very luminous objects. In particular, these authors found that the contribution due to star formation to the total FIR luminosity is, on average, 82%–94% for galaxies with $L_{\mathrm{IR}} < 10^{12.4}\ L_\odot$ (for a cosmology with $H_0 = 75$

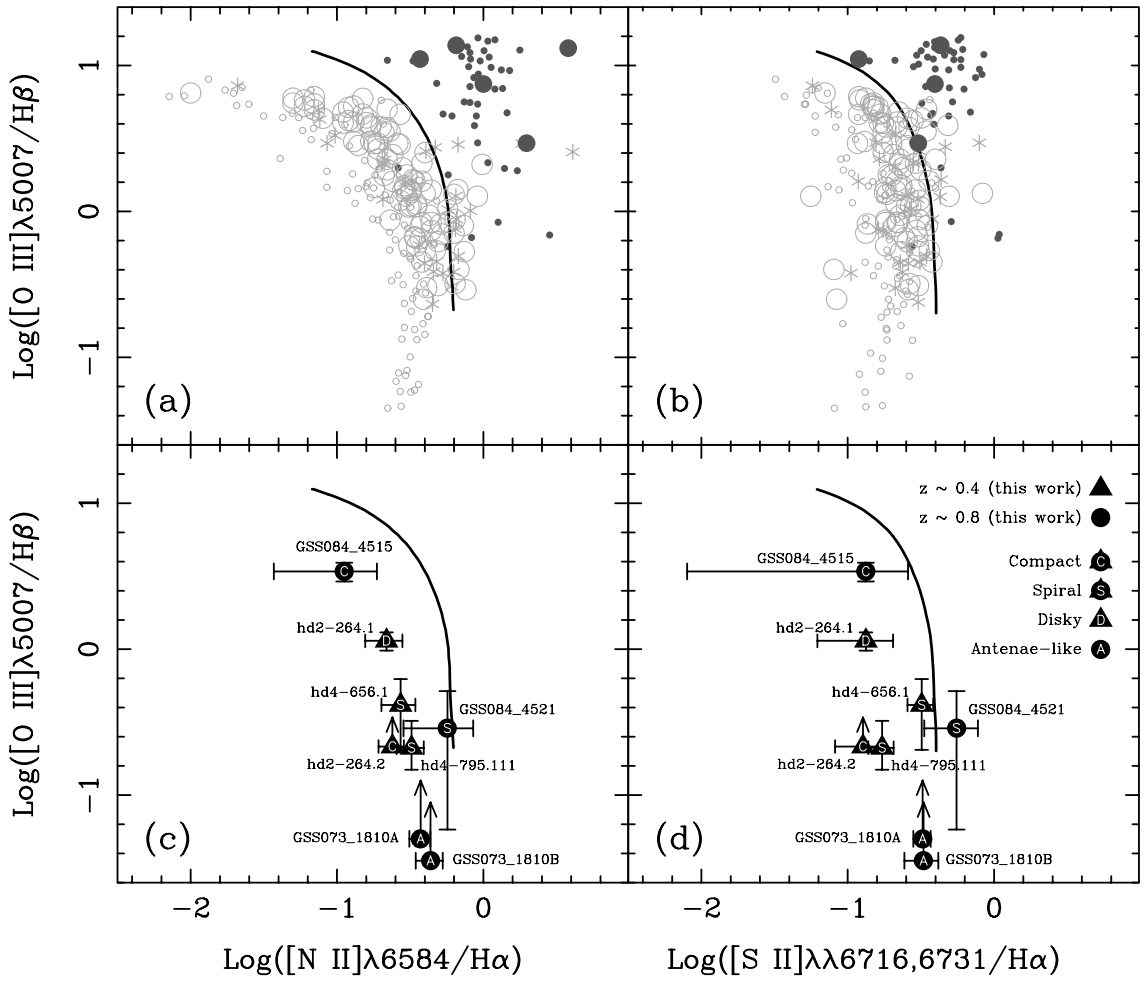

FIG. 5.—Diagnostic diagrams for (*a*) and (*b*) nearby galaxies and (*c*) and (*d*) our galaxy sample. (*a*) and (*b*) *Filled symbols:* galaxies with active nuclei; *open symbols:* galaxies with star formation; *small symbols:* galaxies from Figs. 1 and 2 of VO87 (we only distinguish between emission due to star formation and due to active nuclei; we have also included the objects classified as narrow emission line galaxies by VO87 [*asterisks*], which are either LINERs or H II galaxies); *large symbols:* UCM galaxies from Gallego et al. (1996) (complete sample of Hα emission line galaxies at $z < 0.045$); *thick solid line:* separation between different type of galaxies. There is a small but clear offset between the locus of star-forming galaxies in the VO87 data, when compared with the UCM galaxies. This shift is probably caused by the use by VO87 of data from the literature, which used different slit apertures. (*c*) and (*d*) Emission-line ratios for our galaxy sample after applying extinction corrections (triangles for objects with $z \sim 0.4$, circles for galaxies with $z \sim 0.8$); arrows indicate that the [O III]/Hβ ratio is unknown. In the last two panels we have labeled the symbols with the letters C, S, D, and A to indicate the morphological type of each galaxy, as indicated in the symbol key. Since the [O III] λ5007 line for GSS 084_4521 was outside the spectral range of LRIS, we have estimated its value using the measured [O III] λ4959 flux. In the case of the colliding galaxies GSS 073_1810 both lines were not within the observed spectral interval, so only [N II] λ6583/Hα and [S II] $\lambda\lambda$6716, 6731/Hα are indicated. Both panels indicate that all the galaxies of our sample fall in the region of star-forming galaxies.

TABLE 7

EMISSION-LINE RATIOS AND METALLICITIES

Galaxy	[O III] λ5007/Hβ	[N II] λ6583/Hα	[S II] $\lambda\lambda$6717, 6731/Hα	[N II] λ6583/[O II] λ3727	R_{23}[a]	O_{32}[b]	$12 + \log(O/H)$[c]
hd2-264.1	1.14 ± 0.16	0.22 ± 0.06	0.13 ± 0.07	0.32 ± 0.10	3.40 ± 0.55	0.75 ± 0.14	8.83 ± 0.06
hd2-264.2	>0.21	0.24 ± 0.05	0.13 ± 0.05	0.22 ± 0.04	>3.47	>0.09	8.78 ± 0.06
hd4-656.1	0.41 ± 0.21	0.27 ± 0.07	0.32 ± 0.06	0.31 ± 0.08	3.09 ± 0.29	0.22 ± 0.09	8.84 ± 0.04
hd4-795.111	0.21 ± 0.06	0.32 ± 0.07	0.17 ± 0.03	0.67 ± 0.15	1.66 ± 0.16	0.20 ± 0.05	9.00 ± 0.02
GSS 073_1810A	...	0.37 ± 0.06	0.32 ± 0.04	0.43 ± 0.07	...	...	...
GSS 073_1810B	...	0.44 ± 0.09	0.33 ± 0.09	0.75 ± 0.14	...	...	...
GSS 084_4515	3.41 ± 0.50	0.11 ± 0.08	0.13 ± 0.12	0.07 ± 0.05	9.48 ± 1.37	1.03 ± 0.05	8.33 ± 0.11
GSS 084_4521[d]	0.29 ± 0.23	0.57 ± 0.28	0.55 ± 0.22	0.83 ± 0.40	2.34 ± 0.81	0.19 ± 0.14	8.92 ± 0.10

NOTE.—All the emission-line fluxes have been corrected for extinction.

[a] $R_{23} \equiv$ ([O II] λ3727 + [O III] $\lambda\lambda$4959, 5007)/Hβ.

[b] $O_{32} \equiv$ ([O III] $\lambda\lambda$4959, 5007)/[O II] λ3727.

[c] Errors correspond to the propagation of the emission-line flux uncertainties when deriving the metallicities from the R_{23} and O_{32} indices (see Fig. 10*a*). However, additional uncertainties associated with the use of this empirical calibration are $\pm$0.15 dex (Kobulnicky et al. 1999).

[d] The [O III] λ5007 flux for this galaxy has been determined from [O III] λ4959.

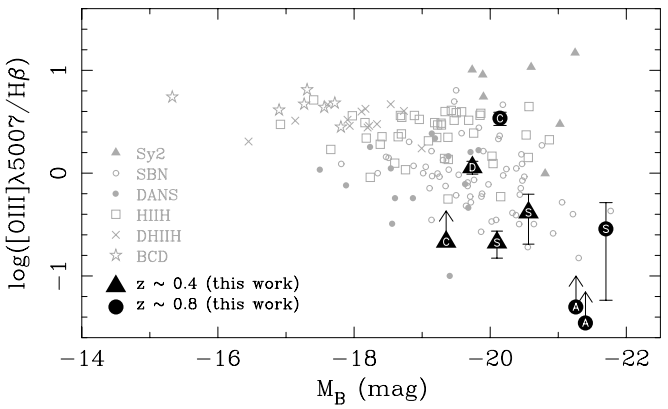

FIG. 6.—Excitation as a function of rest-frame absolute blue magnitude for the galaxies in our sample (*large symbols*, labeled as in Fig. 5), compared to the sample of nearby UCM ($z < 0.045$) emission-line galaxies of Gallego et al. (1996, 1997) (*small symbols*). The rest-frame absolute *B* magnitudes for the VCM sample have been extracted from the data presented by Pérez-González et al. (2002) and were corrected for Galactic extinction using the dust maps of Schlegel et al. (1998). Different symbols are employed to show the classification of the local galaxies of different types (see discussion in §3).

km s^{-1} Mpc^{-1} and $q_0 = 0.5$); these numbers decrease to 44%–55% at higher luminosities. Considering that all our galaxies are below that threshold (see Table 8), our data support the idea that star formation is the dominant source of ionization in our sample (note that the largest L_{IR} value of $\sim 10^{12}\ L_\odot$ corresponds to GSS 073_1810, which actually consists of two interacting galaxies).

Since accretion around black holes must lead to the formation of luminous X-ray sources, especially in the hard X-ray domain (less sensitive to extinction affecting obscured AGNs), the cross-correlation of deep X-ray and MIR observations is a direct way to check for the mechanism responsible for the nebular emission lines. From the deep X-ray survey in the HDF-N performed with *Chandra* (Hornschemeier et al. 2000, 2001; Brandt et al. 2001), we find that only one of our four galaxies in this field, hd2-264.1, is an X-ray source (see Fig. 5 in Brandt et al. 2001). Very recently Fadda et al. (2002) have studied in detail the mechanisms that power the X-ray emission of ISOCAM galaxies in the HDF-N+FF presenting X-ray counterparts. They found that hd2-264.1 exhibits an X-ray luminosity $L_X \sim 2 \times 10^{41}$ ergs s^{-1} and an X-ray spectral index similar to those of the star-forming galaxies Arp 220 and Arp 244. Although we are not going to repeat all the details here, it is important to stress that the latter result alone clearly suggests that, in spite of its X-ray detection, a dominant AGN contribution in this object can be safely dismissed.

Further support to the idea that the optical light of the galaxies under study is dominated by hot stars is given by the LRIS spectra of the GSS subsample. These have enough S/N that a cross-correlation of their SED against well-known SEDs of local star-forming galaxies is easily done. This task was carried out by fitting the continuum regions free of high sky line residuals to the SEDs in the spectrophotometric atlas of Kennicutt (1992b) masking out emission-line regions. One of the best fits is obtained with NGC 4775, a typical Sc galaxy. This result, shown in Figure 7, reveals that typical high-order absorption Balmer lines, a signature of young stellar populations, are present in the spectra of these targets.

A final piece of data gives more support to the same idea: the measured emission-line widths are not broad. The averaged FWHM values (derived from the fits to the emission lines with better S/N and without high residuals of sky lines), after quadratically subtracting the spectral resolution, are 110 ± 9 (hd2-264.1), 94 ± 9 (hd2-264.2), 101 ± 7 (hd4-656.1), 129 ± 9 (hd4-795.111), 216 ± 26 (GSS 073_1810A), 167 ± 45 (GSS 073_1810B), 327 ± 42 (GSS 084_4515), and 216 ± 35 km s^{-1} (GSS 084_4521). With this result, we are confident that none of the galaxies under study are Seyfert 2 galaxies.

In conclusion, although we cannot completely rule out AGNs as a possible source of ionizing radiation, all evidence compiled here suggests that such a contribution, if present, is very small.

TABLE 8

ADDITIONAL GALAXY PROPERTIES

Galaxy	M_B[a]	R_e (kpc)[b]	Mass ($M_\odot$)[c]	L_{IR} ($L_\odot$)[d]
hd2-264.1	−19.7	$5.69^{+2.63}_{-0.24}$	4.8×10^{10}	$10^{10.57}$
hd2-264.2	−19.4	$1.02^{+0.44}_{-0.40}$	1.2×10^{10}	$<10^{10.48}$
hd4-656.1	−20.6	$3.29^{+0.49}_{-0.11}$	4.4×10^{10}	$10^{10.13}$
hd4-795.111	−20.1	$2.63^{+0.93}_{-0.21}$	3.9×10^{10}	$10^{10.09}$
GSS 073_1810A	−21.3	$5.76^{+0.11}_{-0.08}$	...	...
GSS 073_1810B	−21.4	$3.92^{+0.27}_{-0.10}$	...	...
GSS 073_1810	−22.1	...	...	$10^{11.97}$
GSS 084_4515	−20.1	$2.45^{+0.28}_{-0.12}$	...	$<10^{11.59}$
GSS 084_4521	−21.7	$4.24^{+0.27}_{-0.05}$	...	$10^{11.59}$

[a] Rest-frame absolute magnitudes in the *B* band (AB system), derived as explained in § 5.

[b] Half-light radii, computed as explained in § 5.

[c] Galaxy masses, derived as explained in § 5.

[d] Total IR luminosity, $L_{IR} = L(8\text{–}1000\ \mu\text{m})$. These numbers have been derived as explained in § 4.3.

4. MULTIWAVELENGTH STAR FORMATION RATES

We have transformed the previous flux measurements and their corresponding errors (Tables 2, 4, and 5) into SFRs, using well-known calibrations. The summary of this computation is presented in Table 9, displayed in Figure 8, and described in this section.

4.1. SFR *from Ultraviolet Continua*

Since the resulting UV spectrum of star-forming galaxies is roughly flat in the range of 1500–2800 Å, the SFR can be derived from any measurement of the UV luminosity in that spectral interval, using a calibration such as that given in equation (1) of Kennicutt (1998), namely,

$$\mathrm{SFR_{UV}}\left(M_\odot\ \mathrm{yr}^{-1}\right) = 1.4 \times 10^{-28} L_{\mathrm{UV}}\left(\mathrm{ergs\ s^{-1}\ Hz^{-1}}\right). \quad (1)$$

Note that at the mean redshifts of the HDF-N and GSS galaxies of our sample, the *U*-band magnitudes displayed in Tables 4 and 5—the *HST* F300W ($\langle\lambda\rangle \sim 3000$ Å) and the KPNO *U* ($\langle\lambda\rangle \sim 3670$ Å) filters—sample practically the same rest-frame wavelength $\lambda_{\mathrm{rest}} \sim 2050$ Å. The estimated luminosities were corrected for internal reddening using the recipe of Calzetti et al. (2000) for starbursts, where the color excesses for the stellar continuum were derived using $E(B-V)_{\mathrm{cont}} = 0.44E(B-V)_{\mathrm{gas}}$ (Calzetti 1997). In addition,

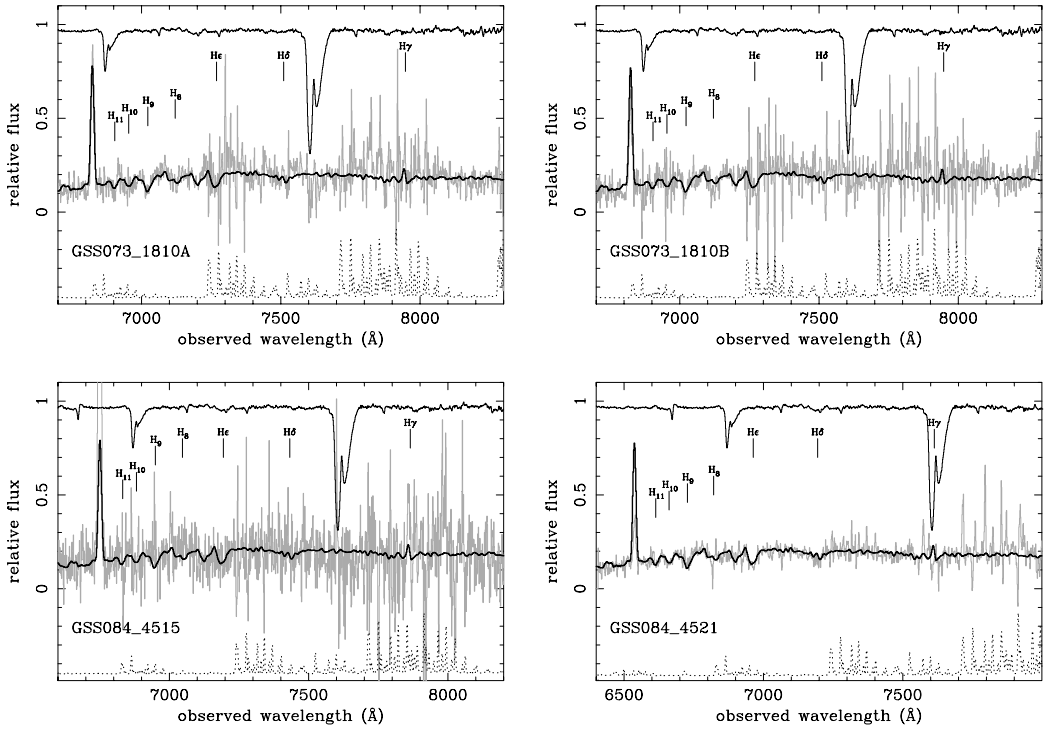

FIG. 7.—Comparison of the GSS subsample spectra with a local Sc galaxy spectrum. The thin line (*light gray*) is the spectrum of each galaxy (in arbitrary units); the upper spectrum is the normalized atmospheric transmission; the dotted line is the corresponding sky spectrum (in arbitrary units and shifted downward); the thick line is the spectrum of NGC 4775, a typical Sc galaxy from the spectrophotometric atlas of Kennicutt (1992b), redshifted and scaled to match the continuum level of each galaxy spectrum. The wavelength locations of the Balmer lines present in the plotted spectral range are also shown. Note that, in spite of the unavoidable large residuals associated with bright sky lines, there is good agreement between the GSS spectra and the scaled Sc spectrum. Since in all the panels the SED of NGC 4775 is plotted with the same scale, the different strength of [O II] λ3727 reveals that the GSS galaxies span a range in the equivalent width of this emission line.

the Galactic extinction has been corrected using the $E_G(B-V)$ from Table 1 and the extinction curve of Fitzpatrick (1999).

The errors were determined numerically by bootstrapping the original spectra and their corresponding error spectra. Thus, the bootstrap propagates the errors in $E(B-V)_{\rm gas}$ quoted in Table 2. However, we have not included here the intrinsic scatter in equation (1). In fact, different calibrations between UV flux and SFR differ by $\sim$0.3 dex (Kennicutt 1998). In addition, systematic errors may also be present as a result of the fact that equation (1) is valid only for galaxies with continuous star formation over timescales of 10^8 or longer.

4.2. SFR *from* [O II] *and* Hα *Luminosities*

Here we use the average calibrations given in equations (3) and (2) of Kennicutt (1998),

$$\mathrm{SFR}_{[\mathrm{O\,II}]}\left(M_\odot\ \mathrm{yr}^{-1}\right) = 1.4\times10^{-41}L_{[\mathrm{O\,II}]}\left(\mathrm{ergs\ s}^{-1}\right) \quad (2)$$

TABLE 9

SFR ESTIMATES ($M_\odot$ yr^{-1}) CORRECTED FOR EXTINCTION AND APERTURE EFFECTS

Galaxy	$\mathrm{SFR}_{\rm UV}$	A(UV)[a] (mag)	$\mathrm{SFR}_{[\mathrm{O\,II}]}$	A([O II])[a] (mag)	$\mathrm{SFR}_{\mathrm{H}\alpha}$	A(Hα)[a] (mag)	$\mathrm{SFR}_{\rm IR}$	$\mathrm{SFR}_{\rm radio}$
hd2-264.1	$1.2^{+0.8}_{-0.5}$	$1.5^{+0.6}_{-0.5}$	$4.4^{+3.8}_{-2.0}$	$1.7^{+0.7}_{-0.6}$	$3.6^{+1.6}_{-1.1}$	$0.88^{+0.34}_{-0.32}$	$6.4^{+3.3}_{-2.4}$	11 ± 4
hd2-264.2	$5.1^{+2.0}_{-1.4}$	$2.2^{+0.4}_{-0.3}$	$7.1^{+3.5}_{-2.3}$	$2.6^{+0.4}_{-0.4}$	$3.6^{+0.9}_{-0.7}$	$1.3^{+0.2}_{-0.2}$	<5.2	<20
hd4-656.1	$2.4^{+0.5}_{-0.4}$	$0.23^{+0.19}_{-0.18}$	$2.8^{+0.7}_{-0.6}$	$0.24^{+0.23}_{-0.23}$	$1.8^{+0.2}_{-0.2}$	$0.12^{+0.12}_{-0.12}$	$2.3^{+1.7}_{-0.5}$	<18
hd4-795.111	$2.7^{+0.7}_{-0.5}$	$0.83^{+0.25}_{-0.25}$	$1.9^{+0.6}_{-0.5}$	$0.97^{+0.31}_{-0.30}$	$2.2^{+0.4}_{-0.4}$	$0.49^{+0.15}_{-0.15}$	$2.1^{+1.4}_{-0.2}$	<16
GSS 073_1810A	...	...	35^{+22}_{-13}	$2.1^{+0.5}_{-0.5}$	$29.8^{+9.8}_{-6.9}$	$1.1^{+0.3}_{-0.2}$	...	...
GSS 073_1810B	...	...	$7.4^{+8.3}_{-3.8}$	$1.1^{+0.8}_{-0.7}$	$9.4^{+5.2}_{-3.1}$	$0.58^{+0.42}_{-0.37}$	...	...
GSS 073_1810[b]	$15.0^{+5.2}_{-3.8}$	$1.4^{+0.3}_{-0.3}$	42^{+23}_{-13}	$1.7^{+0.3}_{-0.4}$	39^{+11}_{-8}	$0.84^{+0.2}_{-0.2}$	161^{+50}_{-55}	$\lesssim86$
GSS 084_4515	$3.1^{+2.6}_{-1.4}$	$0.89^{+0.67}_{-0.66}$	20^{+22}_{-10}	$1.0^{+0.8}_{-0.8}$	$7.4^{+4.3}_{-2.7}$	$0.53^{+0.4}_{-0.4}$	<67	<81
GSS 084_4521	$7.6^{+17.9}_{-4.7}$	$1.6^{+1.4}_{-1.0}$	15^{+50}_{-10}	$1.9^{+1.7}_{-1.2}$	15^{+17}_{-7}	$0.96^{+0.83}_{-0.62}$	67^{+29}_{-35}	94 ± 44

NOTE.—See Fig. 8 for a graphical comparison of these numbers.

[a] Extinction correction factors derived from the color excesses given in Tables 1 and 2 and applied to correct the UV, [O II], and Hα fluxes listed in Table 2 in order to get the SFR values quoted in this table.

[b] $\mathrm{SFR}_{[\mathrm{O\,II}]}$ and $\mathrm{SFR}_{\mathrm{H}\alpha}$ values for this object correspond to the sum of the respective values for the individual galaxies (listed in the previous two entries).

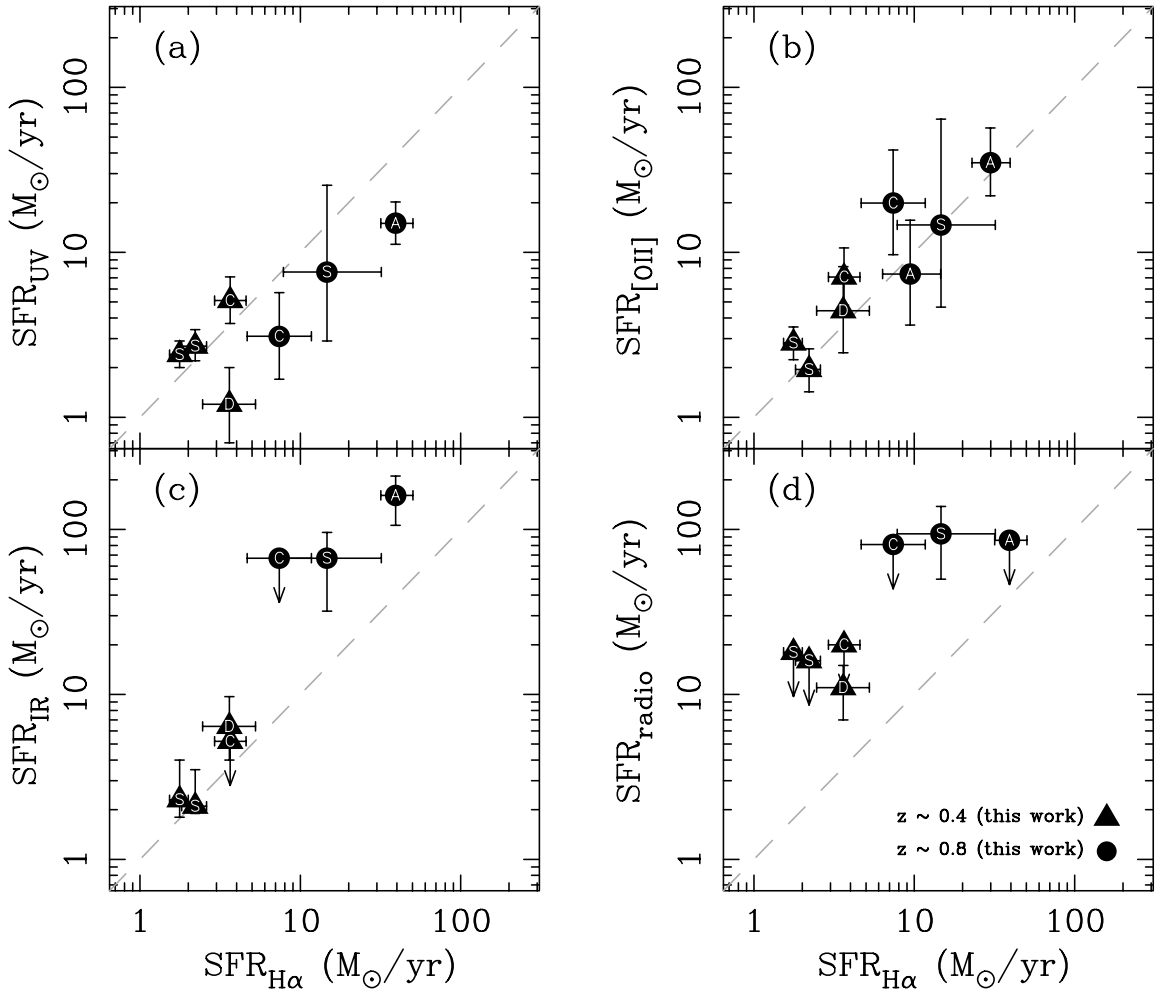

FIG. 8.—Comparison of the five SFR indicators listed in Table 9. Triangles correspond to the HDF-N galaxies ($z \sim 0.4$) and circles to the GSS subsample ($z \sim 0.8$). Symbols are labeled as in Fig. 5. Upper limits in SFR_{IR} and SFR_{radio} are shown with arrows. See discussion in § 7.

and

$$\mathrm{SFR}_{\mathrm{H}\alpha}(M_\odot\ \mathrm{yr}^{-1}) = 7.9 \times 10^{-42} L_{\mathrm{H}\alpha}(\mathrm{ergs\ s}^{-1})\ , \quad (3)$$

where the correction for internal reddening was applied as described above. It is important to keep in mind that $L_{\mathrm{H}\alpha}$ traces the instantaneous SFR because the Hα emission is due to the reprocessing of ionizing radiation shortward of 912 Å, which is produced by the most massive stars. Thus, they are strongly dependent on the adopted initial mass function.

Since the errors in $E(B-V)_{\mathrm{gas}}$ and the extinction-corrected Hα flux are correlated, the error spectra were also bootstrapped to calculate the errors for $SFR_{H\alpha}$. We should also note that in this procedure we have not included the intrinsic scatter in equations (2) and (3).

Finally, the values derived for $SFR_{[O\,II]}$ and $SFR_{H\alpha}$ and their corresponding error bars were corrected for aperture effects. For that purpose, we used the factors listed in Table 3 for the bluest filters. In particular, HDF-N galaxies were corrected using the fraction of galaxy light passing through the U_{300} filter, whereas for the GSS objects we employed the factors associated with the V_{606} filter (slit 1.″18 for $SFR_{[O\,II]}$; slit 0.″76 for $SFR_{H\alpha}$). These aperture-corrected SFRs are the ones tabulated in Table 9.

4.3. SFR *from Mid-Infrared Fluxes*

The SFR of a galaxy may be estimated from its integrated IR luminosity, $L_{\mathrm{IR}} = L(8\text{–}1000\ \mu\mathrm{m})$, using equation (4) of Kennicutt (1998),

$$\mathrm{SFR}_{\mathrm{IR}}(M_\odot\ \mathrm{yr}^{-1}) = 4.5 \times 10^{-44} L_{\mathrm{IR}}(\mathrm{ergs\ s}^{-1})\ . \quad (4)$$

The IR SED of local star-forming galaxies generally peaks in the FIR, between $\lambda \sim 40$ and 100 μm. In this spectral region, most of the luminosity is due to the thermal emission of the so-called big dust grains. The MIR flux is a combination of broad emission features and hot dust continuum as in the SED of the prototypical starburst galaxy M82 presented in Figure 9*a*. Our sample of galaxies was observed in the LW3 filter of ISOCAM, centered at 15 μm ($\lambda = 12\text{–}18$ μm).

At the redshift of the HDF-N galaxies ($z \sim 0.4$), the ISOCAM LW3 filter (Fig. 9*a*, *upper thick horizontal segment*) samples almost the same rest-frame wavelength as the *IRAS* 12 μm filter for galaxies at $z = 0$. In Figure 9*b* we show that the 12 μm luminosity (νL_ν) of local galaxies is tightly correlated with their integrated IR luminosity, L_{IR}. We used the 293 galaxies from the *IRAS* Bright Galaxy Sample (BGS; Soifer et al. 1989) with 12 μm flux densities and redshifts to derive this correlation.

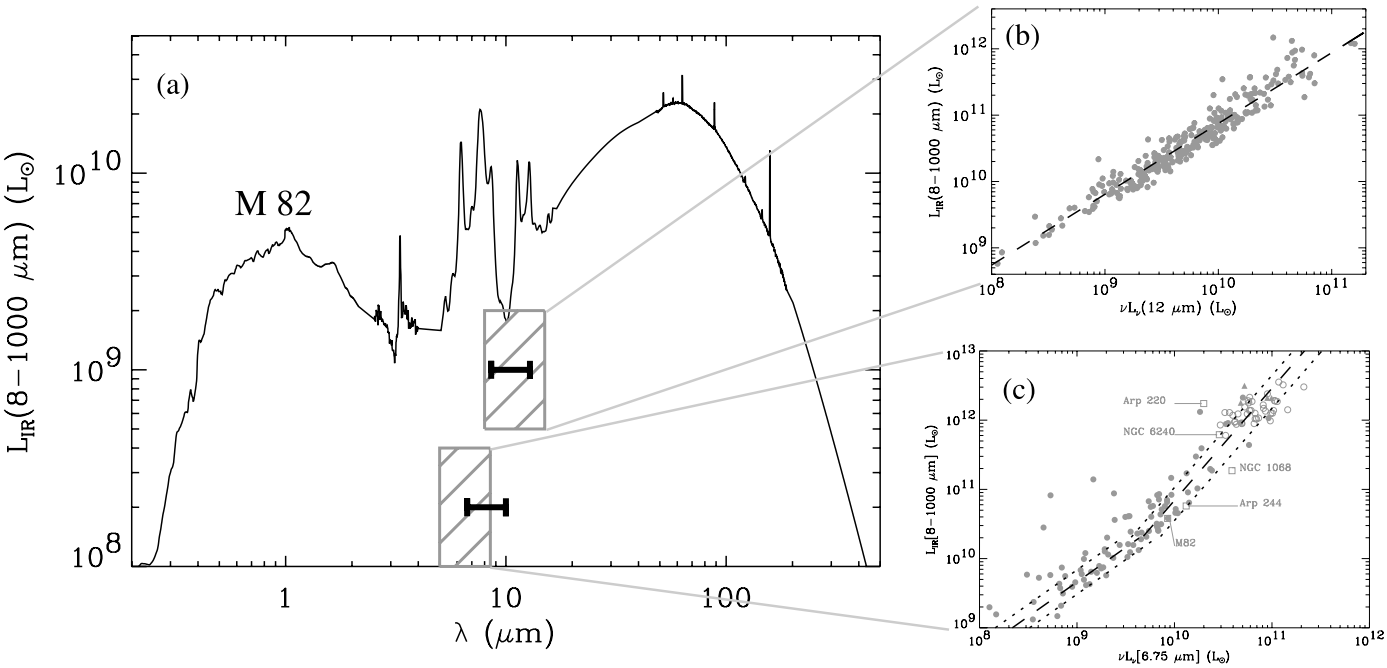

FIG. 9.—(*a*) SED of the prototypical starburst M82 (as in Elbaz et al. 2002). The two thick line segments mark the width and position of the ISOCAM LW3 filter if the galaxy were located at $z = 0.4$ (*upper*) and 0.8 (*lower*). The dashed rectangular regions mark the position and width of the *IRAS* 12 μm filter (*upper*) and ISOCAM LW2 filter (*lower*). (*b*) Integrated IR luminosity, L_{IR}, vs. *IRAS* 12 μm monochromatic luminosity in νL_ν for 293 *IRAS* BGS galaxies. (*c*) Integrated IR luminosity, L_{IR}, vs. ISOCAM LW2 (6.75 μm) monochromatic luminosity in νL_ν. This figure, which contains 91 galaxies, comes from Fig. 5*d* of Elbaz et al. (2002).

At the redshift of the GSS galaxies ($z \sim 0.8$), the ISOCAM LW3 filter (Fig. 9*a*, *lower thick horizontal segment*) largely overlaps the same rest-frame wavelength as the ISOCAM LW2 filter (*lower dashed rectangle*), which is centered at 6.75 μm ($\lambda = 5$–8.5 μm). In Figure 9*c* we have reproduced Figure 5*d* from Elbaz et al. (2002), which shows that rest-frame LW2 luminosities are also correlated with L_{IR}.

The previous two correlations suggest that we can compute L_{IR} for galaxies with $z \sim 0.4$ and 0.8 that were detected at 15 μm. However, because the rest-frame wavelength range corresponding to the observed 15 μm ISOCAM band does not exactly match the ISOCAM LW2 and *IRAS* 12 μm filters, we did not compute L_{IR} directly from the correlations but instead from a library of template SEDs ranging from 0.1 to 1000 μm. These templates were produced by Chary & Elbaz (2001), who combined observed SEDs in order to reproduce the same observed trends between MIR and FIR luminosities derived from ISOCAM, *IRAS*, and SCUBA observations of nearby galaxies.

This computation relies on the hypothesis that the trends observed for local galaxies apply also to galaxies located at $z \sim 0.4$ and 0.8. As suggested in Elbaz et al. (2002), this assumption is supported by the correlation observed between radio and MIR luminosities both in the local and distant universe ($z \sim 0.8$).

To obtain the total integrated IR luminosity for the galaxies of our sample, we proceeded as follows. We computed the expected flux density, $S_\nu(15\ \mu m)$, for all the template SEDs, at the redshifts of each of our sample galaxies. The values thus obtained were compared to the measured ISOCAM 15 μm flux densities in order to select, for each sample galaxy, the template SED that best matched its ISOCAM flux density. The chosen SED was then used to predict *IRAS* flux densities. The latter were employed to compute the total IR flux densities, using

$$\frac{F_{IR}(\mathrm{W\ m^{-2}})}{1.8 \times 10^{-14}} = 13.48 f_{12} + 5.16 f_{25} + 2.58 f_{60} + f_{100} \quad (5)$$

(Sanders & Mirabel 1996), where f_{12}, f_{25}, f_{60}, and f_{100} are the *IRAS* flux densities in Jy at 12, 25, 60, and 100 μm, respectively.

Note that we did not compute L_{IR} by directly integrating the template SED because the SEDs of Chary & Elbaz (2001) were built to fit correlations using equation (5). Anyway, the difference in the computation of L_{IR} between using equation (5) and integrating the SED is of the order of only 5%–10%. The final IR luminosity for each galaxy is listed in Table 8.

The error bars in SFR_{IR} quoted in Table 9 have been computed by propagating the errors in the ISOCAM 15 μm flux [i.e., obtaining the best SED that fitted $S_\nu(15\ \mu m) \pm$ error]. They do not include a possible intrinsic scatter within the correlations shown in Figures 9*b* and 9*c* since the observed scatter combines this intrinsic scatter with measurement errors. If the scatter observed in Figures 9*b* and 9*c* were mostly intrinsic, the 1 σ error bars on SFR_{IR} quoted in Table 9 should be increased according to a 40% uncertainty on L_{IR}.

4.4. SFR *from Radio Fluxes*

The correlation between radio and IR luminosities (Helou, Soifer, & Rowan-Robinson 1985; Condon, Anderson, & Helou 1991; Yun, Reddy, & Condon 2001) offers an additional diagnostic tool to estimate the SFR. This correla-

tion can be characterized with the help of the flux density ratio q defined by Helou et al. (1985),

$$q = \log\left[\frac{F(40\text{–}120\ \mu\text{m})}{3.75 \times 10^{12}\ \text{W m}^{-2}}\right] - \log\left[\frac{S_\nu(1.4\ \text{GHz})}{\text{W m}^{-2}\ \text{Hz}^{-1}}\right], \quad (6)$$

where $S_\nu(1.4\ \text{GHz})$ is the observed 1.4 GHz flux density in units of W m^{-2} Hz^{-1}. In the study of a complete sample of 1809 galaxies from the *IRAS* 2 Jy sample, Yun et al. (2001) have shown that 98% of the galaxies follow the above relation with $q = 2.34 \pm 0.01$, the scatter in the linear relation being $\sim$0.26 dex.

We computed rest-frame radio luminosities at 1.4 GHz assuming that $S_\nu \propto \nu^{-\alpha}$ (as suggested by Yun et al. 2001), using the radio fluxes given in Table 6 and the typical radio spectral index $\alpha = 0.80 \pm 0.15$, with the exception of hd2-264.1 ($\alpha = 0.87 \pm 0.12$) and GSS 084_4521 ($\alpha = 0.75 \pm 0.25$), whose values were determined more precisely as a result of the availability of radio measurements at two different frequencies.

To convert the derived FIR luminosity, L(40–120 μm), into integrated IR luminosity, L(8–1000 μm), we used the following tight correlations derived from the *IRAS* BGS (Soifer et al. 1989):

$$L(8\text{–}1000\ \mu\text{m}) = (1.26 \pm 0.15)L(40\text{–}500\ \mu\text{m}), \quad (7)$$

$$L(40\text{–}500\ \mu\text{m}) = (1.50 \pm 0.10)L(40\text{–}120\ \mu\text{m}), \quad (8)$$

and thus

$$L(8\text{–}1000\ \mu\text{m}) = (1.89 \pm 0.26)L(40\text{–}120\ \mu\text{m}). \quad (9)$$

Finally, the $\text{SFR}_{\text{radio}}$ is computed from equation (4), employing the L(8–1000 μm) luminosity obtained from the combination of equations (6) and (9).

The random errors correspond to the co-added effect of random errors in the radio flux and in the spectral index α, neglecting the contribution of a possible intrinsic scatter in the q parameter.

5. ADDITIONAL GALAXY PROPERTIES

Although the galaxy sample examined in this paper is small, it is clear from Figure 1 that it includes a diverse collection of objects. In addition to SFR estimates, the sample can also be used to derive additional galaxy properties, like metallicities and masses, which will provide a more complete description of each object.

Metallicities can be determined from the measured emission-line strengths using the empirical line flux ratio technique of Pagel et al. (1979), which relates the line ratio

$$R_{23} = \frac{[\text{O II}]\ \lambda3727 + [\text{O III}]\ \lambda\lambda4959,\ 5007}{\text{H}\beta} \quad (10)$$

to the oxygen abundance O/H. This calibration, shown in Figure 10*a*, can be parameterized as a function of the

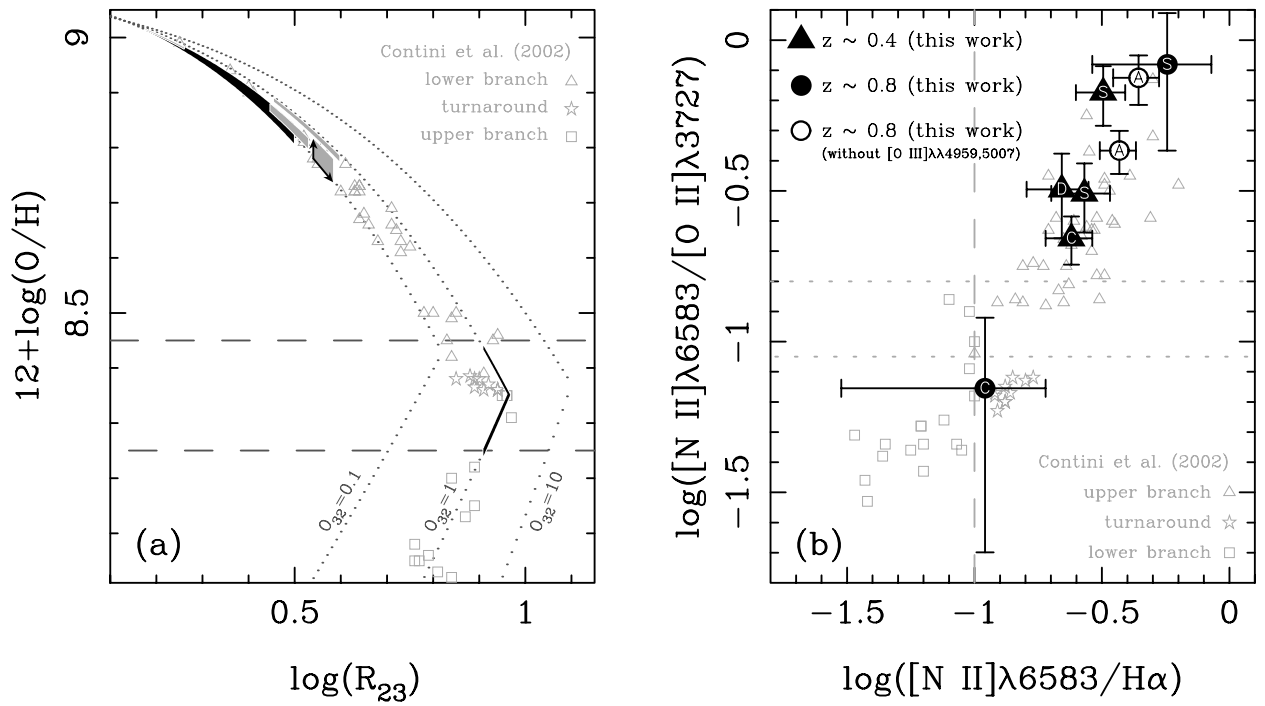

FIG. 10.—(*a*) Calibration of oxygen abundance, as a function of the line ratio $R_{23} \equiv ([\text{O II}]\ \lambda3727 + [\text{O III}]\ \lambda\lambda4959,\ 5007)/\text{H}\beta$ and parameterized by the ionization parameter $O_{32} \equiv ([\text{O III}]\ \lambda\lambda4959,\ 5007)/[\text{O II}]\ \lambda3727$. The dotted lines correspond to the analytic fits by Kobulnicky et al. (1999) to the McGaugh (1991) set of photoionization models. The shaded areas are the galaxies of our sample (lighter regions galaxies at $z \sim 0.4$; for hd2-264.2 we only have lower limits in R_{23} and O_{23}, which have opposite effects in metallicity, as shown by the arrows). The dashed lines mark the turnaround region, where the uncertainties are large. Data points come from Fig. 4 of Contini et al. (2002): open squares and triangles discriminate between the lower and upper branches, whereas the open stars are objects that fall in the intermediate region. (*b*) Diagnostic diagram employed to break the degeneracy in (*a*). We have also included in this diagram the galaxy sample of Contini et al. (2002), which illustrates the method for breaking the degeneracy of the oxygen abundance as a function of the R_{23} index: triangles correspond to their galaxies that fall on the upper branch of the R_{23} calibration [$\log([\text{N II}]\ \lambda6583/\text{H}\alpha) > -1$ and $\log([\text{N II}]\ \lambda6583/[\text{O II}]\ \lambda3727) > -1.05$], squares to objects that lie on the lower branch [$\log([\text{N II}]\ \lambda6583/\text{H}\alpha) < -1$ and $\log([\text{N II}]\ \lambda6583/[\text{O II}]\ \lambda3727) < -0.8$], whereas stars correspond to galaxies that fall in the turnaround region of the calibration. As is clear from this figure, the metallicity for the galaxies of our sample must be read from the upper branch calibration of (*a*), except for GSS 084_4515, which lies in the intermediate region.

ionization parameter

$$O_{32} = \frac{[\text{O III}]\ \lambda\lambda 4959,\ 5007}{[\text{O II}]\ \lambda 3727}\ . \qquad (11)$$

In this work we have adopted the analytic fits of Kobulnicky, Kennicutt, & Pizagno (1999)—in particular, their equations (7)–(9)—to the set of photoionization models of McGaugh (1991). As seen in Figure 10*a*, these calibrations are degenerate, there being two widely different oxygen abundances for a given pair of R_{23} and O_{32} values. Fortunately, the diagnostic diagram relating [N II] λ6583/[O II] λ3727 with [N II] λ6583/Hα (see Fig. 10*b*) has proven to be an excellent tool for breaking this degeneracy, as shown by Contini et al. (2002). In particular, galaxies that fall in the upper right quadrant of this diagram can be safely assigned to the upper branch (high metallicity) of the oxygen calibration in Figure 10*a*. This is the case for all galaxies in our sample, except GSS 084_4515, which falls in the turnaround region of the calibration diagram. Even though the measures for this galaxy present large uncertainties, it is clear that it exhibits the lowest metallicity. We have also included in Figures 10*a* and 10*b* the UV-selected galaxies from Contini et al. (2002) to illustrate the reliability of this method. The R_{23} and O_{32} metallicity indicators, together with the final derived metallicities, are listed in Table 7. Note that for the two colliding galaxies GSS 073_1810 the [O III] $\lambda\lambda$4959, 5007 emission lines fall, unfortunately, outside the observable wavelength range of LRIS, so we cannot derive their metallicity. However, the location of these two objects in Figure 10*b* (shown as open circles) suggests that they also should have a metallicity corresponding to the upper branch of the R_{23} calibration in Figure 10*a*. This result is fully consistent with the position of our galaxies in the excitation diagram presented in Figure 6, in which the local starburst trend is typically interpreted as a sequence governed by the metallicity content of the ionized gas, with metallicity increasing when moving from the H II galaxies to the SBNs.

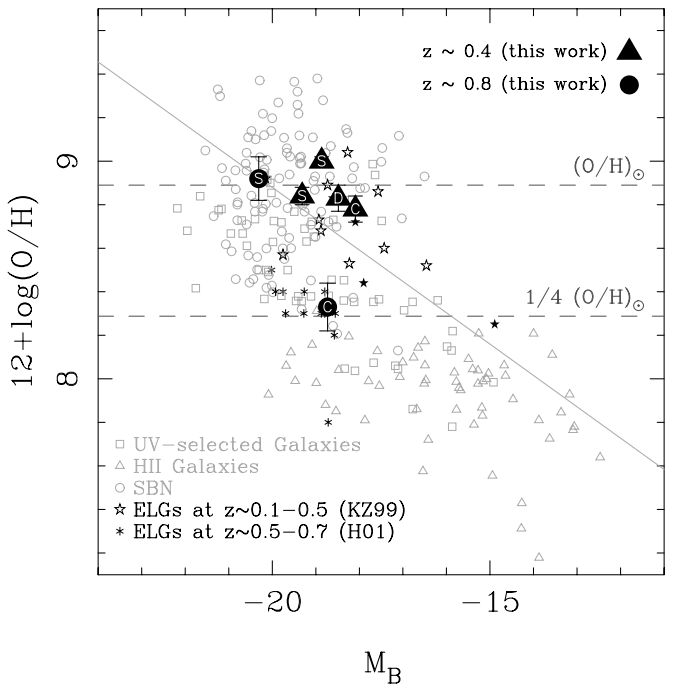

FIG. 11.—Metallicity-luminosity diagram. The different galaxy samples have been extracted from Contini et al. (2002; Fig. 10*a*). Note that in order to perform the comparison, the rest-frame absolute *B* magnitudes of the galaxies of our paper have been transformed to a cosmology with $H_0 = 100$ km s^{-1} Mpc^{-1} and $q_0 = 0.5$. The comparison samples include nonlocal emission-line galaxies from Kobulnicky & Zaritsky (1999; four CNELGs of their sample are represented with filled stars) and 14 LCGs from Hammer et al. (2001). The solid line is the least-squares fit to local irregular and spiral galaxies from Kobulnicky & Zaritsky (1999; Fig. 4).

The locus of our galaxy sample in the metallicity-luminosity diagram is examined in Figure 11 and compared with the regions spanned by additional samples of galaxies, extracted from Figure 10*a* of Contini et al. (2002; see references therein). In this sense, hd2-264.1, hd4-656.1, hd4-795.111, and GSS 084_4521 are perfectly compatible with the locus spanned by local SBN galaxies (*open circles*). In addition, GSS 084_4515 overlaps with the luminous compact galaxies (LCGs) of Hammer et al. (2001), whereas hd2-264.2 is close to the location of the $z \sim 0.1$–0.5 emission-line objects of Kobulnicky & Zaritsky (1999). Finally, since the positions of the two interacting galaxies GSS 073_1810 in Figure 11 indicate that their metallicities are likely to be in the range covered by the remaining spiral galaxies of the sample, and considering their rest-frame absolute *B* magnitude, their location in Figure 11 should also be compatible with the SBN objects.

Galaxy masses for the HDF-N subsample have been estimated using the *K*-band photometry published by Fernández-Soto et al. (1999) and listed in Table 4. Using the SED of late-type galaxies given by Fukugita et al. (1995), we have derived an average *K*-correction of $K(z) - K(0) = -0.65$ mag. Finally, we have employed a mass-to-light ratio 0.93 $M_\odot\ L_{K,\odot}^{-1}$, which is the value for the local SBN-like galaxies modeled by Gil de Paz et al. (2000). The resulting masses are listed in Table 8.

We also quote in Table 8 values for the galaxy half-light radius, which come from the Medium Deep Survey (Ratnatunga, Griffiths, & Ostrander 1999) fits in the F606W filter for HDF-N galaxies (roughly rest-frame *B* band at $z \sim 0.4$) or from GIM2D (Simard et al. 2002) fits to the F814W filter (close to the rest-frame *B* band at $z \sim 0.8$) in the case of GSS galaxies. The uncertainties for the HDF-N data were estimated from the variation of the half-light radius values when using the F300W and F814W filters. The errors for the GSS galaxies combine the uncertainties calculated by GIM2D using Monte Carlo simulations, added to the variation in the galaxy fits using the F606W images.

We have combined the computed rest-frame absolute *B* magnitudes with the half-light radii and the emission-line widths to compare the structural properties of our galaxy sample (see Fig. 12) with those of different galaxy types (both local and at redshifts $\lesssim 1$) compiled and published by Phillips et al. (1997). The unambiguous spiral-type galaxies of our sample (hd4-656.1, hd4-795.111, GSS 073_1810, and GSS 084_4521) fall in the region spanned by local galaxies of this type in these figures (since these objects are observed face-on, their positions in Fig. 12*c* are only lower limits). The disky galaxy hd2-264.1 is also compatible with low-luminosity and low-mass spirals, whereas the compact object hd2-264.2 is consistent with the compact narrow emission line galaxy (CNELG) and compact galaxies at higher redshifts of Phillips et al. (1997) and Guzmán et al. (1997). Interestingly, another compact galaxy from our sample, GSS 084_4515, behaves in a rather different fashion when plotted in these diagrams. The latter result is examined in more depth in the next section.

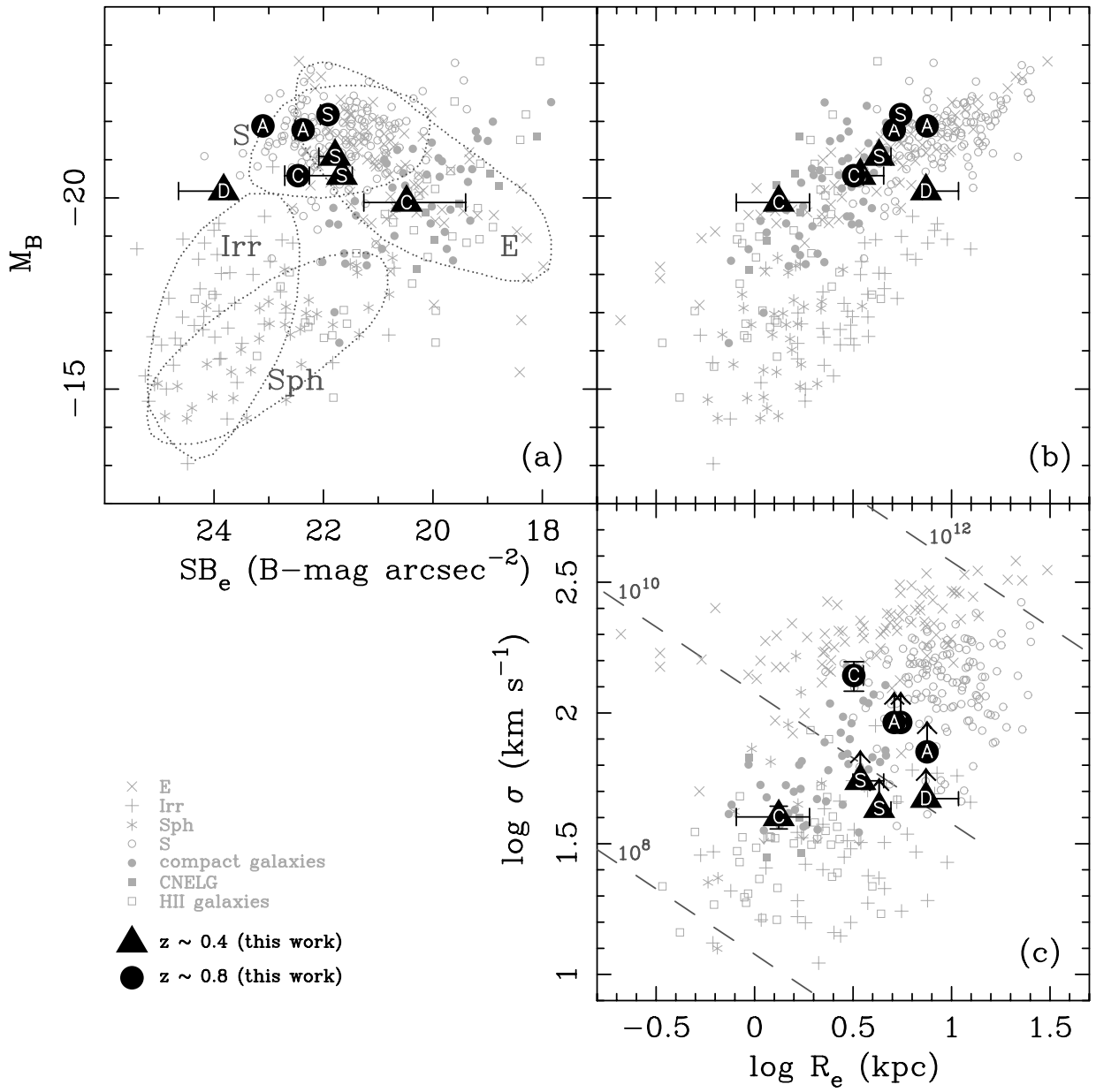

FIG. 12.—Comparison between blue luminosities, half-light surface brightnesses, and velocity widths of our galaxy sample and the data from Phillips et al. (1997). (*a*) Rest-frame surface brightness (averaged within the half-light radius) and blue luminosities. The dotted regions indicate the plot domain spanned by different types of local galaxies. (*b*) Comparison of rest-frame half-light radii and blue luminosities. (*c*) Comparison of rest-frame half-light radii and velocity widths. Since the clear spiral-type galaxies of our sample are viewed almost face-on, we assume that the measured emission-line widths are underestimating the actual rotational velocity of these objects. For that reason they are plotted as lower limits. The dashed lines are isomass tracks (in solar units) corresponding to the virial mass estimation used by Guzmán et al. (1996), $M \simeq 3c_2/G\sigma^2 R_e$, where we have assumed the exponential case $c_2 = 1.6$ for the geometry-dependent parameter. In this comparison we transformed our data to a cosmology with $H_0 = 50$ km s^{-1} Mpc^{-1} and $q_0 = 0.05$.

6. DESCRIPTION OF INDIVIDUAL GALAXIES

Here we present a summary of the properties of each galaxy in our sample.

6.1. hd2-264.1

This galaxy appears to be closely connected with hd2-264.2 (the difference in radial velocity between both objects is only ~350 km s^{-1}), and the star formation episode may well have been triggered as the result of the interaction between both galaxies. In the *HST* images hd2-264.1 shows a central blue condensation and a close to edge-on diffuse disk. Based on the standard emission-line ratio diagnostics, this object qualifies as a starburst nucleus of moderate luminosity ($M_B = -19.7$), similar in Hα luminosity, FIR luminosity, color, and size to the local galaxies in the same spectroscopic category.

6.2. hd2-264.2

This object is a featureless compact galaxy close to hd2-264.1. Its appearance in the *HST* images is highly concentrated, with a half-light radius of ~0.6 kpc in the F300W band and ~1.5 kpc in the F814W band. Its low luminosity and small velocity dispersion indicate a low-mass system where a star-forming process, likely motivated by an interaction with its larger companion hd2-264.1, has increased

its luminosity. Its spectrum confirms those characteristics typical of a high-ionization ongoing star formation process. The object was not detected by *ISO* and shows similar properties to the compact star-forming galaxies at intermediate redshifts studied by different authors (Phillips et al. 1997; Guzmán et al. 1997; Kobulnicky & Zaritsky 1999).

6.3. hd4-656.1

This face-on spiral galaxy exhibits two well-defined spiral arms in the *HST* images. The object shows emission lines that correspond to a moderate starburst in the nucleus. The galaxy properties of this object are similar to those of its local counterparts.

6.4. hd4-795.111

This galaxy has very similar properties, within errors, to those of hd4-656.1. Both show moderate IR luminosities and spectral features consistent with a nuclear starburst, with an SFR of about 2 $M_\odot$ yr^{-1} as indicated by all the SFR tracers.

6.5. GSS 073_1810

The *HST* images of GSS 073_1810 reveal a system formed by two morphologically disrupted spiral galaxies ($\Delta v_r \sim 70$ km s^{-1} in Hα). This large ($\sim$27 kpc total diameter) and luminous system is clearly undergoing a strong burst of star formation. It is worth noting that each individual component could be considered as being average in size and luminosity. The combined system, based on its integrated IR luminosity, can barely be qualified as a ULIRG [$\log(L_{\rm IR}/L_\odot) = 11.97$]. The ratio $\mathrm{SFR_{IR}}/\mathrm{SFR_{H\alpha}}$ is well above the $\sim$1 observed for objects with IR luminosity lower than 10^{11} $L_\odot$, confirming a different nature for the object.

6.6. GSS 084_4515

The behavior of this interesting galaxy differs significantly from hd2-264.2, the other compact object analyzed in this work. It shows the lowest metallicity of the galaxy sample, and its value matches that of the sample of LCGs at $0.5 \lesssim z \lesssim 0.7$ (Fig. 11, *asterisks*) of Hammer et al. (2001). Its mass ($\sim 4 \times 10^{10}$ $M_\odot$, as read from Fig. 12*c*) is also similar to that of the LCG sample (10^{10}–2.5×10^{11} $M_\odot$). GSS 084_4515 has an amorphous but compact morphology (half-light radius $\sim$2.5 kpc), and its spectrum is dominated by a high-ionization starburst that accounts for the H II–like emission line ratios. The colors, SFRs, diagnostic diagrams, Hα luminosity, absolute magnitude, and metallicity all suggest that this galaxy is similar to the brightest compact star-forming galaxies studied by Guzmán et al. (1997), in particular the subsample at $z > 0.7$ classified as disklike.

6.7. GSS 084_4521

This object has the appearance of a bright face-on spiral galaxy, and its spectroscopic properties are typical of systems presenting a nuclear starburst. The observed discrepancies between $\mathrm{SFR_{IR}}$ and $\mathrm{SFR_{radio}}$ with $\mathrm{SFR_{UV}}$, $\mathrm{SFR_{[O\,II]}}$, and $\mathrm{SFR_{H\alpha}}$ suggest that its nuclear starburst is highly obscured. The IR luminosity is very high ($\log L_{\rm IR} = 11.59$) but similar to extreme local objects such as UCM 2250+2427.

7. COMPARISON OF DIFFERENT SFR ESTIMATORS

Although it can be argued that the calibrations adopted in § 4 to derive the SFR estimates listed in Table 9 do suffer from large uncertainties, in this work we are precisely seeking systematic deviations when using the same prescriptions in all the galaxies. The discrepancies found by following this approach must then be understood in terms of processes that violate the hypothesis of a similar star-forming scenario in all the galaxies. Among these, varying star formation histories and differences in the wavelength-dependent extinction corrections are expected to be two of the most important factors. In addition, the detailed modeling of nebular emission from star-forming objects by Charlot & Longetti (2001) shows that the situation is even more complex, since variations in either the zero-age ionization parameter, the gas metallicity, or the effective dust–to–heavy-element ratio introduce scatter in the predicted SFRs.

Even assuming the reduced size of our galaxy sample, the graphic comparison presented in Figure 8 does provide an interesting insight concerning how different star formation indicators behave in galaxies at intermediate redshifts.

7.1. $\mathrm{SFR_{UV}}$ *and* $\mathrm{SFR_{H\alpha}}$

The comparison between $\mathrm{SFR_{UV}}$ and $\mathrm{SFR_{H\alpha}}$ (Fig. 8*a*) shows that for galaxies at $z \sim 0.4$, excluding hd2-264.1, the $\mathrm{SFR_{UV}}$ values are slightly above the 1 : 1 relation. In the specific case of hd2-264.1, the *HST* images suggest that we are observing an almost edge-on disk, so the UV extinction correction might be underestimated and the actual UV flux be slightly higher. Interestingly, all the galaxies at higher redshift ($z \sim 0.8$) exhibit underestimated $\mathrm{SFR_{UV}}$. These results are consistent with the work of Sullivan et al. (2001), who found that the UV/Hα ratio decreases with increasing SFR for galaxies in the redshift range $0 < z < 0.5$, whereas for low-SFR objects the UV luminosities lead to higher SFRs than Hα. Previous observations of distant galaxies, using uncorrected Hα fluxes, had already revealed that the UV flux underestimates the SFR by a factor of a few (Glazebrook et al. 1999; Yan et al. 1999; Moorwood et al. 2000). The origin of this dichotomic behavior has tentatively been attributed to temporal variations in the star formation histories, with episodic and rapid starbursts (Glazebrook et al. 1999; Sullivan et al. 2001). However, Bell & Kennicutt (2001) find this explanation insufficient and argue for an increasing attenuation of the UV emission relative to Hα for higher luminosity galaxies.

7.2. $\mathrm{SFR_{[O\,II]}}$ *and* $\mathrm{SFR_{H\alpha}}$

Although it is well known that the observed (i.e., uncorrected for extinction) [O II]/Hα ratio shows a large scatter in local star-forming galaxies (a factor of $\sim$7), this scatter improves when extinction-corrected values are used (Jansen, Franx, & Fabricant 2001; Aragón-Salamanca et al. 2002). In our case (Fig. 8*b*) the comparison between both SFR estimates is, at first sight, quite good within error bars. However, it is interesting to note that the galaxy that deviates the most from the 1 : 1 relation is precisely the object with lowest metallicity, namely, GSS 084_4515. That metallicity is an underlying cause of scatter when comparing [O II] λ3727 with Hα luminosities has been suggested by Jansen et al. (2001). To explore this issue in greater detail, we compare in Figure 13 the correlation found by these authors between

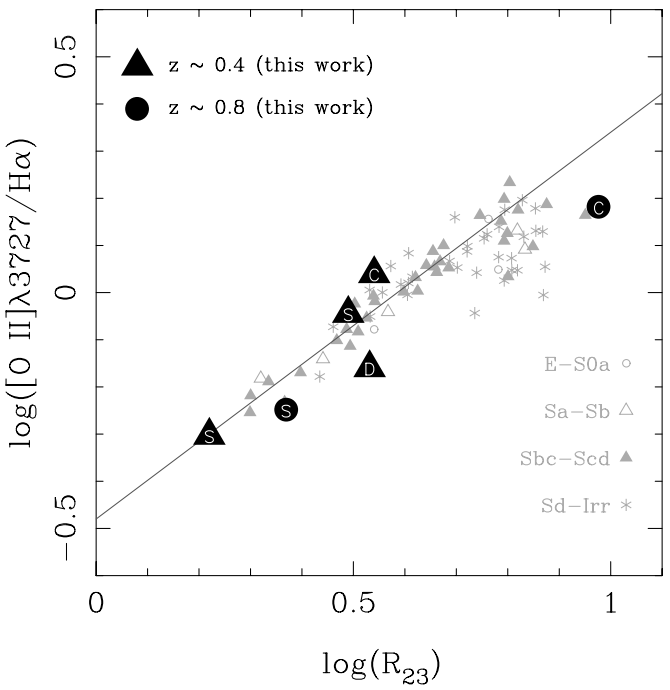

FIG. 13.—Reddening-corrected [O II] $\lambda 3727/\mathrm{H}\alpha$ ratio as a function of the metallicity parameter R_{23}. Small symbols correspond to local galaxies from Jansen et al. (2001), and the full line is a linear fit to these data. The galaxies of our sample do follow very well the same relation.

the [O II]/Hα ratio and the metallicity parameter R_{23} for local emission-line galaxies that are not dominated by an AGN. The solid line is the linear fit to the local galaxy sample, which is given by (Jansen et al. 2001)

$$\log([\mathrm{O\ II}]/\mathrm{H}\alpha) = 0.82 \log R_{23} - 0.48 \ . \qquad (12)$$

The galaxies in our sample follow very well this trend. After applying a metallicity correction to the [O II] SFR estimates (Fig. 14), we find an excellent match between both SFR indicators.

7.3. $\mathrm{SFR_{IR}}$, $\mathrm{SFR_{radio}}$, *and* $\mathrm{SFR_{H\alpha}}$

Finally, in Figures 8*c* and 8*d* we compare the unbiased $\mathrm{SFR_{IR}}$ and $\mathrm{SFR_{radio}}$ estimators with $\mathrm{SFR_{H\alpha}}$. For the two galaxies of our sample with radio detections, $\mathrm{SFR_{IR}}$ and $\mathrm{SFR_{radio}}$ agree very well within the error bars. The remaining upper limits in radio fluxes also give consistent results with the IR data, excluding GSS 073_1810, for which the IR flux is unexpectedly higher than the constraint imposed by the radio flux. For the latter galaxy, an inspection of the radio map of Fomalont et al. (1991; Fig. 2, northwest quadrant) reveals that there is indeed a detection (displayed as an isocontour at a level of 8 μJy) at the expected location of this object. The fact that it constitutes an interacting system with a physical star-forming extension that is likely larger than that exhibited by a single galaxy like GSS 084_4521 might explain why GSS 073_1810 does not present a concentrated peak flux density above the 16 μJy threshold used by Fomalont et al. (1991) to generate their "complete" catalog. Thus, the integrated flux density for this object is probably very close to the sensitivity limit of their survey. This result, together with the uncertainty in the total IR luminosity, lessens the discrepancy between $\mathrm{SFR_{IR}}$ and $\mathrm{SFR_{radio}}$ for this object.

The most intriguing result, which is especially manifest in Figure 8*c*, is the good agreement between these SFR indicators for the galaxy subsample at $z \sim 0.4$, while for the higher redshift (and more luminous) objects the agreement is very poor. To investigate this paradoxical behavior in greater detail, we compare in Figure 15 the ratio $\mathrm{SFR_{IR}}/\mathrm{SFR_{H\alpha}}$ as a function of the IR luminosity. In this diagram we have included additional galaxy samples, both local and at high redshift. The small open symbols correspond to local star-forming galaxies from Gallego et al. (1996) and Buat et al.

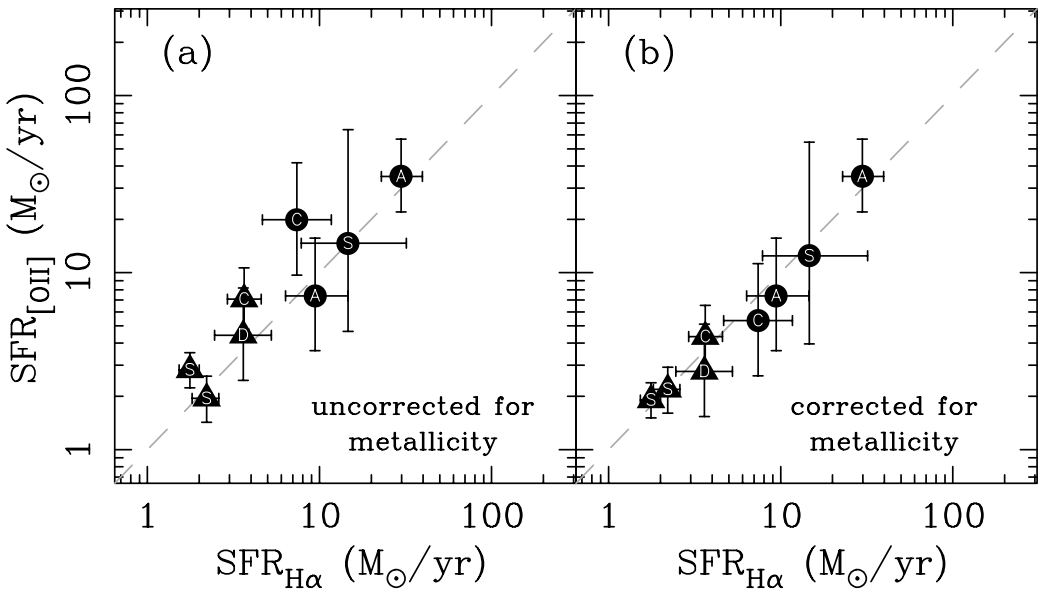

FIG. 14.—Comparison between the SFRs derived from [O II] and Hα luminosities (*a*) without any further correction and (*b*) employing the metallicity correction $\log([\mathrm{O\ II}]/\mathrm{H}\alpha) = 0.82 \log R_{23} - 0.48$ (Jansen et al. 2001) shown in Fig. 13. Note that although for the Antenna-like object (the pair of galaxies GSS 073_1810) we have applied no correction since R_{23} is unknown, the locus of this system in Fig. 10*b* suggests that its R_{23} parameter should be close to that of GSS 084_4515, hd4-656.1, and hd4-795.111, for which the metallicity corrections in this diagram are small.

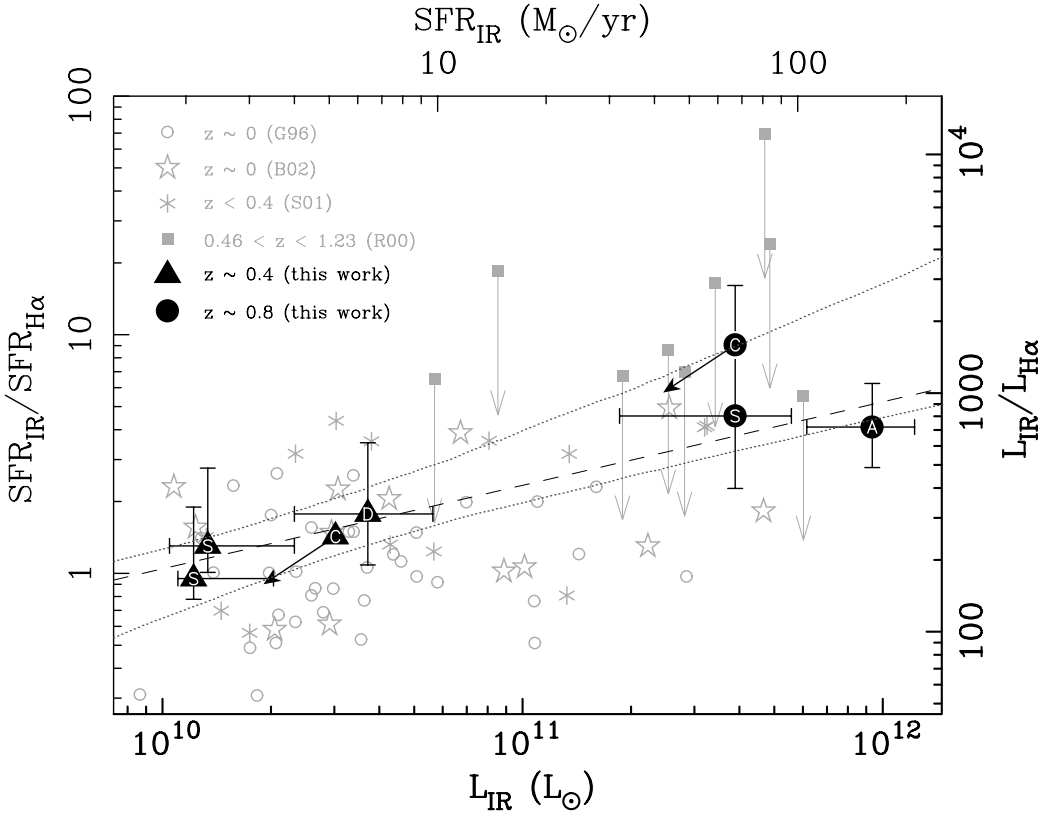

FIG. 15.—Ratio of SFR_{IR} vs. extinction-corrected $SFR_{H\alpha}$, as a function of L_{IR}; the horizontal scale at the top gives the SFR_{IR} as computed from eq. (4). Large filled symbols are the galaxies of our sample (triangles for objects with $z \sim 0.4$, circles for galaxies with $z \sim 0.8$; symbols labeled as in Fig. 5), with $SFR_{H\alpha}$ corrected for extinction and aperture as explained in the text. Small filled squares are the galaxies observed by Rigopoulou et al. (2000) in the HDF-S: the data points correspond to the values without extinction correction, while the tips of the arrows indicate the effect of using the average extinction correction (a factor of 4 in the Hα flux) employed by Rigopoulou et al. (2000) in their work; the Hα fluxes in this last sample were not corrected either for aperture effects. Asterisks are the extinction-corrected objects from Fig. 3*a* of Sullivan et al. (2001), whereas open circles and stars correspond to local galaxies from Gallego et al. (1996, 1997) and Buat et al. (2002, excluding cluster galaxies and objects with apparent diameter larger than 1.″5); respectively. The dashed line is a bisector least-squares fit to our galaxy sample, excluding upper limits in L_{IR} (in both axes), whereas the dotted lines indicate the 1 σ error in the fit prediction derived from numerical simulations via error bootstrapping.

(2002) (excluding cluster galaxies and objects with apparent diameters larger than 1.″5, likely affected by aperture effects). The small filled squares represent the measurements of galaxies observed by Rigopoulou et al. (2000) in the HDF-S without a correction for internal extinction. By including the average extinction correction of these authors (a factor of 4 in the Hα flux), their measurements are displaced to the positions indicated by the tip of the arrows. The Hα fluxes in the latter sample were also not corrected for aperture effects. We have ignored two galaxies from the Rigopoulou sample, namely, ISOHDF-S_38 and ISOHDF-S_39, because they are probable AGNs (both exhibit very strong [N II] lines compared with Hα; see their Fig. 1). Asterisks are the extinction-corrected objects from Figure 3*a* of Sullivan et al. (2001), where we have determined L_{IR} from their 1.4 GHz luminosities using the relations shown in § 4.4 (we have excluded upper limits in Sullivan et al. 2001 data). The dashed line is a bisector least-squares fit (Isobe et al. 1990) to our galaxy sample,

$$SFR_{IR}/SFR_{H\alpha} \simeq 3.3 \times 10^{-4} (L_{IR}/L_{\odot})^{0.35}, \qquad (13)$$

where we have excluded the upper limits in L_{IR} (and thus in $SFR_{IR}/SFR_{H\alpha}$). Our lower redshift ($z \sim 0.4$) galaxies are compatible with the local reference sample, in the sense that $SFR_{H\alpha}$ traces almost all the SFR (if not all) as derived from the IR luminosity. However, this is not true when the more luminous galaxies are considered. In particular, only one object out of 10 local galaxies with $L_{IR} > 10^{11}\ L_{\odot}$ falls above the relation given in equation (13). On the contrary, and although the actual extinctions for the high-redshift sample of Rigopoulou et al. (2000) are unknown, the averaged correction estimated by these authors seems to accommodate their galaxies in the previous fit. Finally, the two most luminous IR objects from the sample of Sullivan et al. (2001) do also appear quite close to the same fit. Summarizing, the data we have collected here indicate that the extinction-corrected $SFR_{H\alpha}$ estimates in $z \sim 0.8$ galaxies miss an increasing fraction of the total SFR, which is clear evidence of the presence of highly obscured dust-enshrouded star-forming regions within these galaxies. In addition, there is an indication that this underestimate may be a function of L_{IR} (eq. [13]). However, considering the luminosity and redshift segregation of our galaxy sample, we cannot yet preclude an effect due only to z.

Interestingly, the two galaxies with compact aspect, hd2-264.2 and GSS 084_4515, were both undetected by *ISO*, and thus we have only plotted upper limits for these objects in Figure 15. However, it is important to highlight that this common morphology is misleading, since, as we have previ-

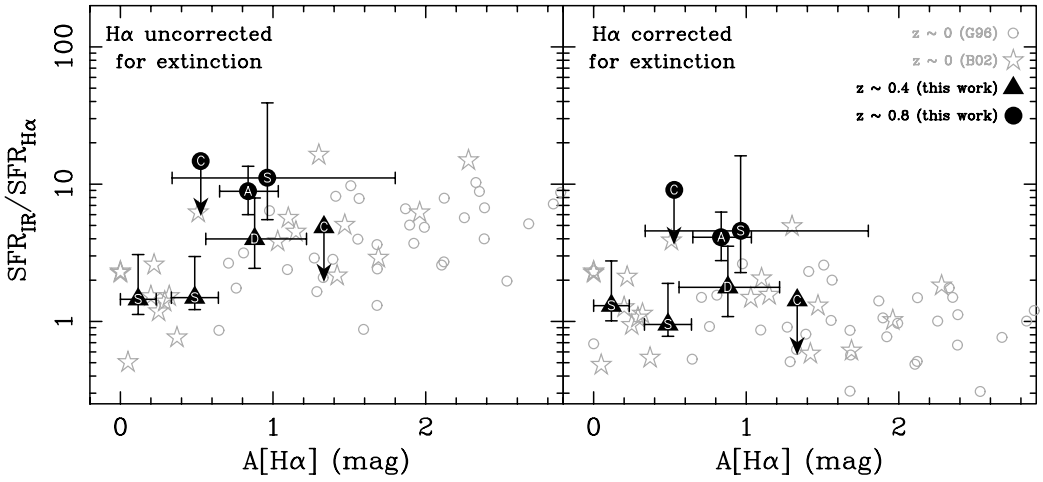

FIG. 16.—Ratio of SFR_{IR} vs. $SFR_{H\alpha}$ (with Hα not corrected for extinction in the left-hand panel and corrected in the right-hand panel) as a function of the measured extinction in Hα. Symbols are the same as in Fig. 15.

ously discussed, these galaxies exhibit different metallicity, mass, and structural properties, apart from a difference of a factor of $\sim$10 in total FIR luminosity. The arrow in hd2-264.2 places this object close to $SFR_{IR}/H\alpha \simeq 1$, whereas in the case of the LCG GSS 084_4515 its real L_{IR} would put it either on the fit given by equation (13) or in the locus of the $z \sim 0.4$ objects. If, as suggested by Hammer et al. (2001), LCGs are evolved starbursts and the progenitors of the present-day spiral bulges, objects of this type may have an important contribution to the SFR density at intermediate redshifts. These authors have also predicted the total FIR luminosities of LCGs to be around $10^{11}\ L_{\odot}$, near or slightly below the limiting sensitivity reached by *ISO* in the redshift range $0.5 \lesssim z \lesssim 0.7$. If we assume that GSS 084_4515 belongs to the same galaxy family, and although its nondetection by *ISO* is then not surprising, this galaxy will be accommodated in the fit of equation (13). This result highlights the relevance of quantifying the actual L_{IR} of LCGs, which will be possible in the near future with the help of *SIRTF*.

Another important question is whether it is possible to use any measurable parameter exclusively derived from the optical lines with the aim of correcting the biased $SFR_{H\alpha}$ estimates, in order to match the values obtained from the total FIR luminosity. In this sense, and as we already mentioned in § 1, Hopkins et al. (2001) and Sullivan et al. (2001) have recently reported a correlation between the optical extinction (derived from the Balmer decrement) and the SFR (or luminosity) of the galaxies. Buat et al. (2002) also find correlations between the measured extinction in Hα, A[Hα], and L_{IR}, although with a very large scatter.

We have represented in Figure 16 the ratio $SFR_{IR}/SFR_{H\alpha}$ as a function of A[Hα]. For local galaxies this ratio correlates with A[Hα] when Hα fluxes uncorrected for extinction are used. After correcting the Hα flux for extinction, local galaxies and our galaxy subsample at $z \sim 0.4$ scatter around $SFR_{IR}/SFR_{H\alpha} \sim 1$, whereas the $z \sim 0.8$ objects remain above this value. Since the measured Hα extinctions in GSS 073_1810 and GSS 084_4521 are very similar, we cannot use this parameter to conclude whether there is any correlation between the systematic underestimation of SFR from Hα as a function of A[Hα]. Anyway, we should note that these two galaxies have Hα extinctions similar to hd2-264.1 and lower than hd2-264.2. Both hd2-264.1 and hd2-264.2 have total FIR luminosities 1 order of magnitude fainter than those of either GSS 073_1810 and GSS 084_4515. For that reason, if there were actually a correlation between the observed rest-frame optical extinction and the ratio $SFR_{IR}/H\alpha$, it should be sought in galaxies with $L_{IR} > 10^{11}\ L_{\odot}$ and, presumably, at intermediate redshifts. Clearly more data are required in order to settle this question.

8. CONCLUSIONS

In this work we have compared several SFR estimators using a small but diverse sample of galaxies at two intermediate redshifts ($z \sim 0.4$ and 0.8). By selecting the sample galaxies on the basis of their ISOCAM 15 μm MIR luminosities, we have sampled SFRs ranging from 2 to 160 $M_{\odot}\ \mathrm{yr}^{-1}$. Their morphological types include spiral, compact, and merging emission-line galaxies. It is important to highlight that the redshift segregation of the sample is also accompanied by a segregation in total FIR luminosity, with the farthest galaxies being the most luminous. This fact leads to an ambiguity between luminosity and distance that must be kept in mind when interpreting the results.

The observed spectral range includes the most prominent optical emission lines, from [O II] λ3727 to [S II] $\lambda\lambda$6716, 6731. The availability of Hβ and Hα allows the determination of color excesses in the nebular gas and correcting the emission-line fluxes for extinction. The diagnostic diagrams generated from the corrected emission-line ratios confirm the star-forming nature of the galaxies, as was already suggested by evidence from their total FIR luminosity, observations in the X-ray domain, and the absence of broad emission lines. In addition, the overall characteristics of the selected galaxies, in particular their metallicity and structural properties, also match those of star-forming galaxies, both local and at intermediate redshifts.

The good agreement between *HST* and ground-based photometry on the one hand and the spectrophotometric calibration of the spectra on the other allow us to be confident about the reliability of the estimated aperture corrections, the final optical emission line luminosities, and thus the SFRs obtained from them. Our results have shown the following:

1. There is a general good agreement in the comparison between the five available SFR indicators (from UV, [O II], Hα, IR, and radio luminosities) for the $z \sim 0.4$ ($L_{IR} < 10^{11}$ $L_{\odot}$) galaxies, whereas the situation is not the same in the case of the $z \sim 0.8$ ($L_{IR} > 10^{11}$ $L_{\odot}$) subsample, the discrepancies being different depending on the considered SFR estimator. Focusing on the $z \sim 0.8$ galaxies, the SFRs derived from UV, [O II], and IR luminosities are, respectively, lower than, similar to, and higher than the values obtained from Hα. The paradoxical behavior of SFR_{UV} versus $SFR_{H\alpha}$ is still a subject of debate, and among the possible explanations for the observed discrepancies are temporal variations in the star formation history and luminosity-dependent attenuations of the UV emission. From the observational perspective, we confirm the findings of Sullivan et al. (2001) and extend their result up to $z \sim 0.8$.

2. The correction for metallicity of the [O II]/Hα ratio (using the relation found in local galaxies) greatly improves the concordance between the SFRs derived from the extinction-corrected luminosities of both emission lines. The correction does in fact work for the galaxies in our sample in the two redshift (or luminosity) bins.

3. The fit given in equation (13) and shown in Figure 15 indicates that *extinction-corrected* $SFR_{H\alpha}$ estimates in LIRGs at intermediate redshifts miss an increasing fraction of the total SFR and that the degree of underestimation increases with L_{IR}. This result confirms the finding by Rigopoulou et al. (2000), who used an averaged extinction correction of $\sim$4 derived from $V-K$ colors. In this work we quantify more rigorously this effect by employing line fluxes corrected for extinction making use of color excesses computed from the Balmer decrement. Thus, there is here an observational evidence that the Balmer emission lines, Hα and Hβ, do not probe the same region of a galaxy as the one that is responsible for the strong IR luminosity in the case of LIRGs. This is even more remarkable in Figure 16, where galaxies with very different SFRs share the same A[Hα]. The spatial resolution in the MIR is not sufficient to confirm this statement at these redshifts, but the case of the Antennae galaxy NGC 4038/4039 (Mirabel et al. 1998) offers a perfect example of such behavior in the local universe. A possible explanation for this effect is that a fraction of the star formation in these galaxies is embedded in dense and opaque dust clouds and that this fraction increases with the total star formation. As already expected, galaxy encounters (hd2-264.1 and hd2-264.2) and mergers (GSS 073_1810) are the likely causes for triggering star formation episodes. Whether a quantitative estimation of the hidden star formation is definitely inaccessible to rest-frame optical spectroscopic studies, and in particular to the use of the measured Hα extinction, seems unclear and deserves further research work.

Some kind of evolution in galaxies with $L_{IR} > 10^{11}$ $L_{\odot}$ at $z \lesssim 0.4$ cannot be discarded, since, as we have shown in Figure 15, an important fraction of local galaxies with those luminosities does not show such a large underestimation of the SFR when using Hα fluxes instead of FIR luminosities. However, the scarcity of the galaxy samples strongly demands additional observational work in order to settle this point.

The inclusion of two apparently compact galaxies in our sample has allowed us to analyze the relation between the different SFR estimators applied to this kind of object relative to what is measured for spiral-like galaxies. In particular, one of these two objects qualifies as an LCG, with similar properties to those of the LCGs at intermediate redshifts studied by Hammer et al. (2001). Surprisingly, this object may be suffering similar dust-enshrouded star formation processes as galaxies with a very different morphological aspect, like the bona fide spiral GSS 084_4521 or even the Antenna-like colliding system GSS 073_1810. The confirmation of this still speculative result, which has important implications concerning the accurate estimation of the cosmic SFR density at intermediate redshifts, will be possible after the launch of *SIRTF*.

Valuable discussions with Jaime Zamorano, Pablo Pérez-González, and Ranga-Ram Chary are gratefully acknowledged. We thank Hervé Aussel for providing us with the deconvolved ISCOCAM flux for hd2-264.1 and Hector Flores for providing us with his revised ISOCAM fluxes for the GSS galaxies. We are grateful to the staff of the W. M. Keck Observatory for their help during the observations. This research has made use of the SIMBAD database, operated at CDS, Strasbourg, France. Support for this work has been provided by NSF grants AST 95-29028 and AST 00-71198. N. C. acknowledges financial support from a UCM Fundación del Amo Fellowship, a short contract at the University of California at Santa Cruz, and the Spanish Programa Nacional de Astronomía y Astrofísica under grant AYA 2000-977. D. E. wishes to thank the American Astronomical Society for its support through the Chretien International Research Grant and Joel Primack and David Koo for supporting his research through NASA grants NAG 5-8218 and NAG 5-3507. R. P. S. acknowledges support provided by the National Science Foundation through grant GF-1002-99 and from the Association of Universities for Research in Astronomy, Inc., under NSF cooperative agreement AST 96-13615, and CNPq/Brazil, for financial support through grant 200510/99-1. J. G. acknowledges financial support from the Spanish Programa Nacional de Astronomía y Astrofísica under grant AYA 2000-1790.

REFERENCES

Aragón-Salamanca, A., Alonso-Herrero, A., Gallego, J., García-Dabó, C. E., Pérez-González, P. G., Zamorano, J., & Gil de Paz, A. 2002, in ASP Conf. Ser., Star Formation through Time, ed. E. Pérez, R. M. González Delgado, & G. Tenorio-Tagle (San Francisco: ASP), in press (astro-ph/0210123)
Aussel, H., Cesarsky, C. J., Elbaz, D., & Starck, J. L. 1999, A&A, 342, 313
Balzano, V. A. 1983, ApJ, 268, 602
Bell, E. F., & Kennicutt, R. C., Jr. 2001, ApJ, 548, 681
Bertin, E., & Arnouts, S. 1996, A&AS, 117, 393
Blain, A. W., Smail, I., Ivison, R. J., & Kneib, J. 1999, MNRAS, 302, 632
Bouchet, P., Lequeux, J., Maurice, E., Prévot, L., & Prévot-Burnichon, M. L. 1985, A&A, 149, 330
Brandt, W. N., et al. 2001, AJ, 122, 1
Brunner, R. J., Connolly, A. J., & Szalay, A. S. 1999, ApJ, 516, 563
Buat, V., Boselli, A., Gavazzi, G., & Bonfanti, C. 2002, A&A, 383, 801
Calzetti, D. 1997, in AIP Conf. Proc. 408, The Ultraviolet Universe at Low and High Redshift: Probing the Progress of Galaxy Evolution, ed. W. H. Waller, M. N. Fanelli, J. E. Hollis, & A. C. Danks (Woodbury: AIP), 403
Calzetti, D., Armus, L., Bohlin, R. C., Kinney, A. L., Koorneef, J., & Storchi-Bergmann, T. 2000, ApJ, 533, 682
Calzetti, D., Kinney, A. L., & Storchi-Bergmann, T. 1994, ApJ, 429, 582
Canalizo, G., & Stockton, A. 2001, ApJ, 555, 719
Cardelli, J. A., Clayton, G. C., & Mathis, J. S. 1989, ApJ, 345, 245
Cardiel, N. 1999, Ph.D. thesis, Univ. Complutense de Madrid

Cardiel, N., Gorgas, J., Cenarro, J., & González, J. J. 1998, A&AS, 127, 597
Cardiel, N., et al. 2003, Rev. Mexicana Astron. Astrofis., in press (astro-ph/0205181)
Charlot, S., & Longhetti, M. 2001, MNRAS, 323, 887
Chary, R., & Elbaz, D. 2001, ApJ, 556, 562
Chmielewski, Y. 2000, A&A, 353, 666
Condon, J. J. 1992, ARA&A, 30, 575
Condon, J. J., Anderson, M. L., & Helou, G. 1991, ApJ, 376, 95
Contini, T., Treyer, M.A., Sullivan, M., & Ellis, R. 2002, MNRAS, 330, 75
Cowie, L. L., Songalia, A., & Barger, A. J. 1999, AJ, 118, 603
Cram, L., Hopkins, A., Mobasher, B., & Rowan-Robinson, M. 1998, ApJ, 507, 155
Dole, H., et al. 2001, A&A, 372, 364
Efstathiou, A., et al. 2000, MNRAS, 319, 1169
Elbaz, D., Cesarsky, C. J., Chanial, P., Aussel, H., Franceschini, A., Fadda, D., & Chary, R. R. 2002, A&A, 384, 848
Elbaz, D., et al. 1999, A&A, 351, L37
Epps, H. W., & Miller, J. S. 1998, Proc. SPIE, 3355, 48
Fadda, D., Flores, H., Hasinger, G., Franceschini, A., Altieri, B., Cesarsky, C. J., Elbaz, D., & Ferrando, Ph. 2002, A&A, 383, 838
Fernández-Soto, A., Lanzetta, K. M., & Yahil, A. 1999, ApJ, 513, 34
Fitzpatrick, E. L. 1985, ApJ, 299, 219
———. 1999, PASP, 111, 63
Fixsen, D. J., Dwek, E., Mather, J. C., Bennett, C. L., & Shafer, R. A. 1998, ApJ, 508, 123
Flores, H., et al. 1999, ApJ, 517, 148
Fomalont, E. B., Windhorst, R. A., Kristian, J. A., & Kellerman, K. I. 1991, AJ, 102, 1258
Fukugita, M., Shimasaku, K., & Ichikawa, T. 1995, PASP, 107, 945
Gallego, J., Zamorano, J., Aragón-Salamanca, A., & Rego, M. 1995, ApJ, 455, L1
Gallego, J., Zamorano, J., Rego, M., Alonso, O., & Vitores, A. G. 1996, A&AS, 120, 323
Gallego, J., Zamorano, J., Rego, M., & Vitores, A. G. 1997, ApJ, 475, 502
Genzel, R., et al. 1998, ApJ, 498, 579
Gil de Paz, A., Aragón-Salamanca, A., Gallego, J., Alonso-Herrero, A., Zamorano, J., & Kauffmann, G. 2000, MNRAS, 316, 357
Glazebrook, K., Blake, C., Economou, F., Lilly, S., & Colless, M. 1999, MNRAS, 306, 843
Groth, E. J., et al. 1994, BAAS, 26, 1403
Guzmán, R., Gallego, J., Koo, D. C., Phillips, A. C., Lowenthal, J. D., Faber, S. M., Illingworth, G. D., & Vogt, N. P. 1997, ApJ, 489, 559
Guzmán, R., Koo, D. C., Faber, S. M., Illingworth, G. D., Takamiya, M., Kron, R. G., & Bershady, M. 1996, ApJ, 460, L5
Hammer, F., Gruel, N., Thuan, T. X., Flores, H., & Infante, L. 2001, ApJ, 550, 570
Hauser, M. G., et al. 1998, ApJ, 508, 25
Helou, G., Soifer, B. T., & Rowan-Robinson, M. 1985, ApJ, 298, L7
Hogg, D. W., Cohen, J. G., Blandford, R., & Pahre, M. A. 1998, ApJ, 504, 622
Hopkins, A. M., Connolly, A. J., Haarsma, D. B., & Cram, L. E. 2001, AJ, 122, 288
Hopkins, A. M., Connolly, A. J., & Szalay, A. S. 2000, AJ, 120, 2843
Hornschemeier, A. E., et al. 2000, ApJ, 541, 49
———. 2001, ApJ, 554, 742
Howarth, I. D. 1983, MNRAS, 203, 301
Isobe, T., Feigelson, E. D., Akritas, M. G., & Babu, G. J. 1990, ApJ, 364, 104
Jansen, R. A., Franx, M., & Fabricant, D. 2001, ApJ, 551, 825
Kawara, K., et al. 2000, in Lecture Notes in Physics 548, *ISO* Survey of a Dusty Universe, ed. D. Lemke, M. Stickel, & K. Wilke (Heidelberg: Springer), 49
Kennicutt, R. C., Jr. 1992a, ApJ, 388, 310
———. 1992b, ApJS, 79, 255
———. 1998, ARA&A, 36, 189
Kobulnicky, H. A., Kennicutt, R. C., Jr., & Pizagno, J. L. 1999, ApJ, 514, 544
Kobulnicky, H. A., & Zaritsky, D. 1999, ApJ, 511, 118
Koo, D. C., et al. 1996, ApJ, 469, 535
Lagache, G., Abergel, A., Boulanger, F., Desert, F.-X., & Puget, J.-L. 1999, A&A, 344, 322
Lagache, G., Haffner, L. M., Reynolds, R. J., & Tufte, S. L. 2000, A&A, 354, 247
Laurent, O., et al. 2000, A&A, 359, 887
Lilly, S. J., Le Fevre, O., Hammer, F., & Crampton, D. 1996, ApJ, 460, L1
Madau, P., Ferguson, H. C., Dickinson, M. E., Giavalisco, M., Steidel, C. C., & Fruchter, A. 1996, MNRAS, 283, 1388
Matsuhara, H., et al. 2000, in Lecture Notes in Physics 548, *ISO* Survey of a Dusty Universe, ed. D. Lemke, M. Stickel, & K. Wilke (Heidelberg: Springer), 106
McCall, M. L., Rybski, P. M., & Shields, G. A. 1985, ApJS, 57, 1
McGaugh, S. S. 1991, ApJ, 380, 140
McLean, I. S., et al. 1998, Proc. SPIE, 3354, 566
Mirabel, I. F., et al. 1998, A&A, 333, L1
Moorwood, A. F. M., van der Werf, P. P., Cuby, J. G., & Oliva, E. 2000, A&A, 362, 9
O'Donnell, J. E. 1994, ApJ, 422, 158
Oke, J. B., et al. 1995, PASP, 107, 375
Osterbrock, D. E. 1989, Astrophysics of Gaseous Nebulae (Mill Valley: University Science Books)
Pagel, B. E. J., Edmunds, M. G., Blackwell, D. E., Chun, M. S., & Smith, G. 1979, MNRAS, 189, 95
Pérez-González, P. G., Zamorano, J., Gallego, J., & Gil de Paz, A. 2000, A&AS, 141, 409
Phillips, A. C., et al. 1997, ApJ, 489, 543
Poggianti, B. M., & Wu, H. 2000, ApJ, 529, 157
Prévot, M. L., Lequeux, J., Maurice, E., Prévot, L., & Rocca-Volmerange, B. 1984, A&A, 132, 389
Puget, J.-L., et al. 1996, A&A, 308, L5
Ratnatunga, K. U., Griffiths, R. E., & Ostrander, E. J. 1999, AJ, 118, 86
Rhodes, J., et al. 1994, AAS, 191, 03.01
Richards, E. A., Kellermann, K. I., Fomalont, E. B., Windhorst, R. A., & Partridge, R. B. 1998, AJ, 116, 1039
Rigopoulou, D., et al. 2000, ApJ, 537, L85
Rousselot, P., Lidman, C., Cuby, J. G., Moreels, G., & Monnet, G. 2000, A&A, 354, 1134
Rowan-Robinson, M., et al. 1997, MNRAS, 289, 490
Salzer, J. J., McAlpine, G. M., & Boroson, T. A. 1989, ApJS, 70, 479
Sanders, D. B., & Mirabel, I. F. 1996, ARA&A, 34, 749
Sanders, D. B., Soifer, B. T., Elias, J. H., Madore, B. F., Matthews, K., Neugebauer, G., & Scoville, N. Z. 1988, ApJ, 325, 74
Savage, B. D., & Mathis, J. S. 1979, ARA&A, 17, 73
Schlegel, D. J., Finkbeiner, D. P., & Davis, M. 1998, ApJ, 500, 525
Seaton, M. J. 1979, MNRAS, 187, 73P
Sheinis, A. I., Bolter, M., Epps, H. W., Kibrick, R. I., Miller, J. S., Radovan, M. V., Bigelow, B. C., & Sutin, B. M. 2002, PASP, 114, 851
Simard, L., et al. 1999, ApJ, 519, 563
———. 2002, ApJS, 142, 1
Smail, I., Ivison, R. J., Blain, A. W., & Kneib, J.-P. 2002, MNRAS, 331, 495
Soifer, B. T., Boehmer, L., Neugebauer, G., & Sanders, D. B. 1989, AJ, 98, 766
Soifer, B. T., & Neugebauer, G. 1991, AJ, 101, 354
Steidel, C. C., Adelberger, K. L., Giavalisco, M., Dickinson, M., & Pettini, M. 1999, ApJ, 519, 1
Stevenson, C. C. 1994, MNRAS, 267, 904
Sullivan, M., Mobasher, B., Chan, B., Cram, L., Ellis, R., Treyer, M., & Hopkins, A. 2001, ApJ, 558, 72
Sullivan, M., Treyer, M. A., Ellis, R. S., Bridges, T. J., Milliard, B., & Donas, J. 2000, MNRAS, 312, 442
Sutin, B. M. 1997, Proc. SPIE, 2871, 1116
Tran, Q. D., et al. 2001, ApJ, 552, 527
Tresse, L., & Maddox, S. J. 1998, ApJ, 495, 691
Treyer, M. A., Ellis, R. S., Milliard, B., Donas, J., & Bridges, T. J. 1998, MNRAS, 300, 303
Veilleux, S., & Osterbrock, D. E. 1987, ApJS, 63, 295 (VO87)
Williams, R. W., et al. 1996, AJ, 112, 1335
Wolberg, G. 1990, Digital Image Warping (Los Alamitos: IEEE Comput. Soc. Press)
Yan, L., McCarthy, P. J., Freudling, W., Teplitz, H. I., Malumuth, E. M., Weymann, R. J., & Malkan, M. A. 1999, ApJ, 519, L47
Yun, M. S., Reddy, N. A., & Condon, J. J. 2001, ApJ, 554, 803